BEAM STEERABLE RECONFIGURABLE ANTENNA WITH SMART RF SWITCHING ON 3D PARASITIC LEVEL

by

Mohammad Ababil Hossain

A thesis submitted in partial fulfillment
of the requirements for the degree

of

MASTER OF SCIENCE

in

Electrical Engineering

Approved:

Bedri A. Cetiner, PhD Major Professor	Ryan Davidson, PhD Committee Member
T.C. Shen, PhD Committee Member	Mark R. McLellan, PhD Vice President for Research and Dean of the School of Graduate Studies

UTAH STATE UNIVERSITY
Logan, Utah

2017

ABSTRACT

Beam Steerable Reconfigurable Antenna with Smart RF Switching on 3D Parasitic Level

by

Mohammad Ababil Hossain, Master of Science

Utah State University, 2017

Major Professor: Bedri A. Cetiner, PhD
Department: Electrical and Computer Engineering

In this thesis, the design, analysis, characterization and fabrication of beam steerable multi-functional reconfigurable antenna (MRA) based on 3-dimensional parasitic layer is reported at 5 GHz. The antenna system consists of a dipole antenna at the center which is surrounded by parasitic spiral metallic pixels on the sides, and conformal tetragonal pixels arranged pyramidically on top and bottom of a 3D printed domed hexagonal supporting structure. With a relatively compact geometry, this antenna can steer the omni-directional beam pattern of a dipole antenna in different azimuth and elevation planes in 3D space. It can also work as a typical dipole and yield different diverse directive patterns within the desired frequency range. A maximum directive gain of around 6 dB can be attained for some modes; while satisfactory resonance bandwidth is achieved for all the modes of operation. Initially, several prototypes of the antenna at 2.4 GHz frequency were fabricated and tested for the proof of concept which showed good agreement with the simulation results. After that- the antenna system was redesigned and refabricated for 5 GHz, which is the main focus of this thesis work. The fabricated 5 GHz version of this MRA is mechanically robust where the pixel segments are connected and disconnected by inter-pixel PIN diode switches. Finally, system level performances of the 5 GHz MRA are investigated for 5G heterogeneous networks where small-cell access points are equipped with MRAs. The results show that,

using distributed mode optimization, MRA equipped small-cell systems could provide up to 29% capacity gains and 13% coverage improvements compared to legacy omni-directional antenna equipped systems.

(73 pages)

PUBLIC ABSTRACT

Beam Steerable Reconfigurable Antenna with Smart RF Switching on 3D Parasitic Level

Mohammad Ababil Hossain

Traditional antennas have a lot of limitations as their performance is usually fixed by their initial geometry. On the other hand, modern communication systems are getting way to complicated compared to their earlier counterparts. This necessitates some special types of smart or reconfigurable antennas, which can dynamically adapt to the requirements of the communication systems more effectively. Using conventional single functional antennas is therefore not an efficient approach in these sort of communication systems. Considering all these factors, in this thesis, a beam steerable reconfigurable antenna system is presented that can yield the radiation patterns of multiple antennas with a single structure, necessary for 5G communication. This antenna system occupies comparatively much smaller space and can provide highly directive gain at different directions. It is expected that- in near future, further improvements of this type of antenna system can be performed to pave the way for some additional necessary functions required in modern communication systems.

To my parents, especially my mother, who ingrained a never-ending zeal for education in my nascent mind during my early childhood

ACKNOWLEDGMENTS

I would like to take this opportunity to thank all the people who helped through my MS program. In particular, I want to give special thanks to my advisor, Dr. Bedri A. Cetiner, who guided me thoroughly and gave me valuable suggestions on my research. He supported and encouraged me even when I was not being able to produce necessary outputs in my research. Under his supervision, I learnt some very basic steps to become an independent and successful researcher. Without his continuous support, it would have been impossible for me to finish my MS. He also assisted me greatly to improve my inter-personal communication skills, which is very important along with a strong technical knowledge to become successful in research.

I am also grateful to my other committee members, Dr. Ryan Davidson and Dr. T.C. Shen, for their valuable insight on my work. I also want to thank all my colleagues whom I worked with during past few years, especially- Mehedi, Towfiq and Abdurrzzak. I quickly merged into the group with their selfless help. My heartiest gratitude goes to Dr. Bahceci, who is one of the most self-less and helpful persons I have been with in my whole life. He taught me LaTeX software thoroughly within the shortest possible time. His cordial assistance also enabled me to write the system level part of this thesis properly.

I would like to remember the contribution of my undergraduate supervisor in Bangladesh, Dr. Abdul Matin, who prematurely passed away in July 2014, the time I was about to embark on a new journey to USA for my graduate studies. He is the person who inculcated in me the early love and passion for a very sophisticated topic like Electromagnetics.

Last, but not the least, I would like to acknowledge gratefulness to my parents. Their relentless support since my childhood helped me to keep my motivation level up during the time when I was passing through lean patches in my academic career.

Mohammad Ababil Hossain

CONTENTS

LIST OF TABLES

LIST OF FIGURES

ACRONYMS

RF	Radio Frequency
3D	3-dimentional
ESPAR	Electronically Steerable Passive Array Radiator
Wi-Fi	Wireless Fidelity
MIMO	Multiple Input Multiple Output
EM	Electromagnetic
EBG	Electromagnetic Band-Gap
FAPs	Femto Cell Access Points
MRA	Multi-functional Reconfigurable Antenna
HFSS	High Frequency Structural Simulator
ADS	Advanced Design System
5G	5^{th} Generation
ABS	Acrylonitrile Butadiene Styrene
SRF	Self Resonant Frequency
Varactor	Variable Capacitors
SINR	Signal-to-Interference plus Noise Ratio
eNBs	Base Stations
LTE	Long Term Evolution
RSRP	Reference Signal Received Power
PF	Proportional Fairness
UE	User Equipment
3GPP	3^{rd} Generation Partnership Project

CHAPTER 1

INTRODUCTION

In recent times, multifunctional reconfigurable antennas have drawn great interest among the researchers over the world due to their dynamically changeable frequency and radiation properties with a comparatively concise antenna geometry [1–3]. Some reconfigurable properties of antenna, such as- beam steerability, polarization diversity, frequency tunability etc. have simplified modern communication systems to a great deal. Not only these type of antennas can render multiple functions, but incorporation of reconfigurable antennas in communication systems has made it possible to alleviate traditional channel impairments, such as- channel fading, noise, interference etc. with significant improvement in spectral efficiency.

Beam steerable antennas are necessary for many applications, e.g., small cells, base stations, Wi-Fi, cognitive radio, adaptive MIMO systems etc. For a reconfigurable antenna system, steering the conventional beam pattern of the main radiating antenna is usually performed by reactive loading mechanism where the current distribution on its different parasitic elements are manipulated either through tuning their interconnected reactance as in [4], or modifying their aperture geometry using electronic switches [5]. Beam can also be steered in desired directions by conventional means, i.e., using multiple antenna elements along with phase shifters, usually done in case of phased array [6]. Most of the time this requires complex and costly feed circuitry. Although in the last few decades, some intensive research have been carried out for the development of phased array systems [7, 8]; however, beam steering by reactive loading method is still preferable in many applications owing to its better degrees of freedom and flexibility.

In [9], R. F. Harrington described the theory behind the radiation mechanism of an N-port antenna system by reactive loading principle. ESPAR (Electronically Steerable Passive Array Radiator) antennas generally work following this principle. There are plethora

of examples of beam steerable ESPAR antennas capable of yielding directive gain patterns in azimuth plane in literature [10, 11]. Along with beam steerability, pattern diversity is also an important factor to ponder in these sort of antenna design. By using reconfigurable switched parasitic impedance elements over a ground plane, an increased diversity pattern was obtained in [12]. In all these designs, a distance of around $\lambda/4$ was maintained between the central active antenna element and surrounding parasitic elements, in the process making the overall antenna system unnecessarily larger. Although a comparatively compact sized beam steerable Yagi antenna has been described in [13], it could yield directive beam in azimuth plane only. ESPAR antennas, however, if designed with a ground plane having variable dimension can produce slight variable tilt in elevation plane [14,15]. Unfortunately, beam steering ability of all these types of antennas in 3D space is confined to only above the ground plane. Therefore, finding a proper antenna system that can radiate effectively in 3D space with satisfactory resonance and gain performance is still an ongoing topic of research.

In [16–18], beam steering in elevation plane of a dipole was performed by inducing asymmetric current distribution in the main dipole arm, through the tuning of reactive integrated loads at different segments. But these methods are not that efficient and flexible in terms of directing beam in 3D space, since they mainly suffer from poor impedance matching due to the asymmetric current distribution in the main dipole structure.

With the rapid advancement in modern technology, the application of engineered electromagnetic materials (metamaterials, metasurface etc.) for attaining desirable radiation properties has given a new dimension in antenna research. Multi-band and size miniaturization [19,20], broad-bandwidth [21], enhanced gain performance [22] etc., have been obtained especially for planar types of antennas by using metamaterials. There have been several works on beam steerable metamaterial antennas also. Beam tilting with integrated metamaterial placed in the vicinity of the main radiating antenna element has been performed in [23,24]. In these cases, the unit cells of metamaterial behaved as directors; consequently a tilted beam with an enhanced gain in the desired direction was obtained. By using a

dipole antenna array having progressive phase shifted network implemented on customized EBG (Electromagnetic Band-gap) structures, an improved gain with a tilted beam pattern in elevation plane was obtained in [25]. Despite the fact that the beam tilting and gain performance of these antennas are quite satisfactory, yet their beam steering ability is just fixed by their initial design geometry, and therefore is limited in some specific planes only. Considering the limitations of all these antennas, a reconfigurable antenna with beam steering ability in both azimuth and elevation planes in 3D space can usher in a new era in modern communication systems.

Following the same concept of directors and reflectors used in a circular Yagi-Uda antenna [26], a beam steering multifunctional reconfigurable dipole antenna system based on a 3D parasitic layer having relatively compact spatial side geometry (less than $\lambda/6$) has been presented in this thesis. Depending on its different switch statuses in the parasitic level, the designed antenna can not only yield beam steering in azimuth plane covering whole 360^o, but also can produce around 20^0 beam tilt in elevation plane with satisfactory resonance, gain and front-to-back ratio for all the modes. Apart from these, this antenna can yield monopole-like radiation pattern in both upward and downward directions within the desired range of frequency, and also can produce different directive diversity patterns in both azimuth and elevation planes. In case of all the switches being OFF, it can provide the omni-directional mode of a typical dipole antenna. Two prototypes of the antenna at 2.4 GHz, one with flat top and another with angled top surface arranged pyramidically, have been fabricated and tested. The initial measurement results of the fabricated prototypes showed satisfactory coherence with their simulation results. In those prototypes, the switches were modeled as perfect short and open. Later, the design was shifted to 5 GHz for the final prototype. 5 GHz version of this antenna system has been made operable by smart RF switching having a mechanically more robust structure. This is the primary focus of this thesis.

In the final part, the application of this antenna in 5G communication has been discussed. 5G wireless communications systems are aiming to create a paradigm shift for wire-

less services compared to 4G and earlier predecessors. The low-cost single-element MRA of this work can produce various radiation pattern shapes that can improve the desired link qualities as well as avoid signal emanation towards unintended directions, and thus, it fits very well to the small cell deployment scenarios. To quantify the potential gains, we investigate the system level performance of a typical 5G heterogeneous network where femto cell access points (FAPs) are equipped with the MRAs. We propose a low-complexity and low-overhead distributed mode selection scheme that can determine the appropriate MRA mode in response to the changes in the channel and the user density. The results show that the MRA equipped FAPs could achieve up to 29% capacity and 13% coverage improvements compared to legacy omni-directional antenna equipped small cell systems with minimal complexity and overhead. Our efforts in this work, in a sense, is a step forward in developing a unified approach where antenna design, communications/signal processing and network aspects are seamlessly integrated, and all system parameters (environment, EM wave properties, and communication algorithms) are jointly optimized. This is the key to achieve the challenging 5G throughput and coverage performances.

In summary, the objective of this thesis is as follows:

- Design and optimization of a beam steerable antenna at 5 GHz in Ansys HFSS software
- Characterization of the designed antenna
- Measurement of the fabricated antennas in the laboratory
- Investigating the system level performance of the antenna for 5G communication.

CHAPTER 2

ANTENNA STRUCTURE AND WORKING MECHANISM

The antenna system consists of a driven dipole at the center, which is surrounded by reconfigurable metallic 3D parasitic layer having interconnecting switching circuitry, as illustrated in Fig. 2.1. The parasitic pixel layer is supported by a 3D printed plastic skeleton. Current is induced in the parasitic layer by electromagnetic coupling from the main radiator half-wave dipole antenna. By manipulating the amplitude and phase of the current in different portions of the parasitic layer, beam is steered in different azimuth and elevation planes. Due to high current density close to the dipole feed point [27], it is comparatively easier to get directive beam patterns in azimuth plane by convenient optimization of side parasitic layers around it. However, current near the tip of a dipole is very small, which eventually causes less EM coupling to its top and bottom parasitic layers. This hinders beam steerability in elevation or theta plane in an antenna system consisted of dipole. Therefore, for the purpose of enhancing the current density along top and bottom parasitic layers and thus enabling theta tilt, optimized conformal tetragonal pixels has been used. The description of geometry of the antenna system and its working principle will be described in this section.

2.1 Geometry of the Antenna System

Main Dipole: A half-wave dipole resonant at 4.9 GHz having an impedance bandwidth of around 20% is used as the driven antenna in the center. Amphenol RF (RG-316/U) coaxial cable is used for constructing the dipole. The dipole arms have a diameter of 0.9 mm and length of 13.5 mm (0.23λ). A small feed-gap of 0.15 mm is maintained between the dipole arms to reduce the quadrature component of current that can negatively affect resonance in dipoles or wire type antennas [28]. The fabricated dipole is modeled in HFSS by keeping all its dimensions intact as much as possible to ensure comparable and reliable

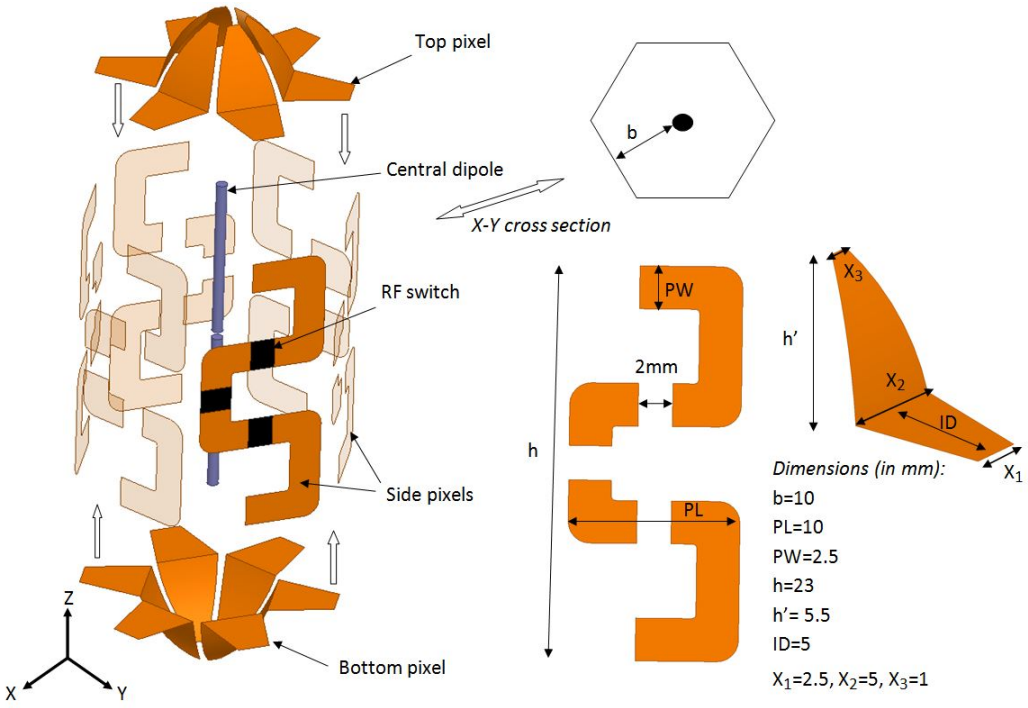

Fig. 2.1: Schematics of the multi-functional reconfigurable antenna.

performances in simulation and measurement. Later that modeled dipole has been used in all later simulation investigations.

3D Printed Supporting Structure: For supporting parasitic elements surrounding the driven dipole, a structure made of ABS (Acrylonitrile Butadiene Styrene) plastic ($\epsilon_r = 2.1$, $\tan\delta = 0.05$) is 3D printed. On top and bottom, it is an inset domed hexagonal structure; while in the middle portion, the 3D printed support has been grooved in such a way so that six rectangular PCBs can be accommodated hexagonally on its six different faces. The electrical and mechanical material properties for 3D printed structure was chosen in such a way so that it can provide necessary mechanical support for the parasitic pixel layers without affecting the antenna performance that much, and each of its size and dimension was fixed based on the optimized dimensions of the metallic parasitic pixel elements.

Parasitic Elements: Spiral shaped parasitic pixel segments having 3 turns with 3 interconnected switches are placed on the 6 sides of the parasitic structure. The spiral pixels were printed on one side of 0.5 mm thick RO4003C substrate ($\epsilon_r = 3.55$, $\tan\delta = 0.001$);

the dimensions of the spiral pixels are shown in Fig. 2.1. Conformal tetragonal pixels were put on the inset domed surface. Placing conformal pixel on inset domed surface can help in several ways: firstly, inset domed structure controls gain and tilt of elevation modes; and secondly, the flatter inset part can be utilized to place switching circuitry. The optimization procedure of the pixels will be described in Chapter 3.

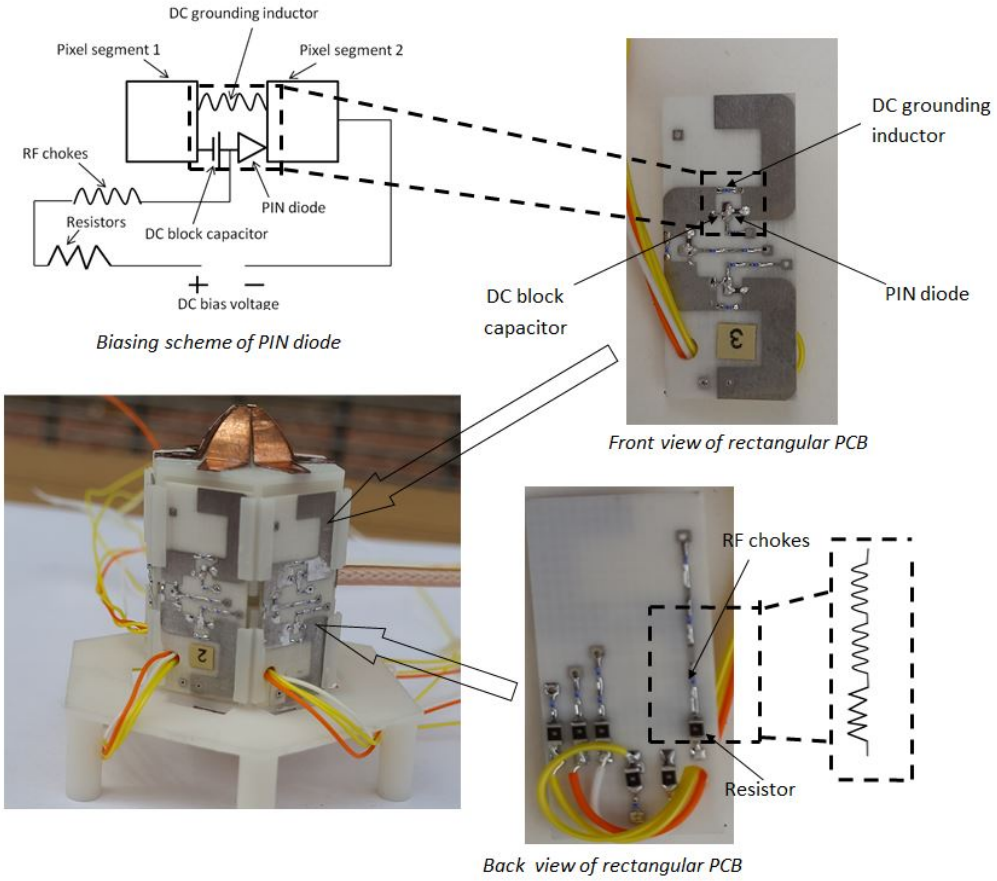

Fig. 2.2: Photograph of the fabricated prototype: Front view of rectangular PCB face with pixels and switching circuitry & back view of rectangular PCB face with bias lines.

Switching Circuitry: PIN diodes are used to interconnect adjacent pixels. The biasing scheme, which is similar to the one used in [29], is also shown in Fig. 2.2 where all pixels are mutually connected by DC grounding inductors. The anode of each PIN diode switch is connected to one pixel and its cathode is connected through a DC-block capacitor to the

adjacent pixel. The biasing lines are located on the back side of the rectangular-shaped microwave laminates and are split in short non-resonant sections by means of RF chokes to minimize their coupling with the pixels as shown in Fig. 2.2. The manufacturer details and properties of the PIN diode and lumped components are shown in Table 2.1. Typically, 1 V DC power supply on the PIN diode would be sufficient to turn on the switch, while 0 V will keep the switch in OFF status. The equivalent circuit models of these lumped components are obtained by using their scattering parameters provided by the manufacturers and are shown in Fig. 2.3. These equivalent circuit models are used in the design of the MRA with reconfigurable radiation patterns.

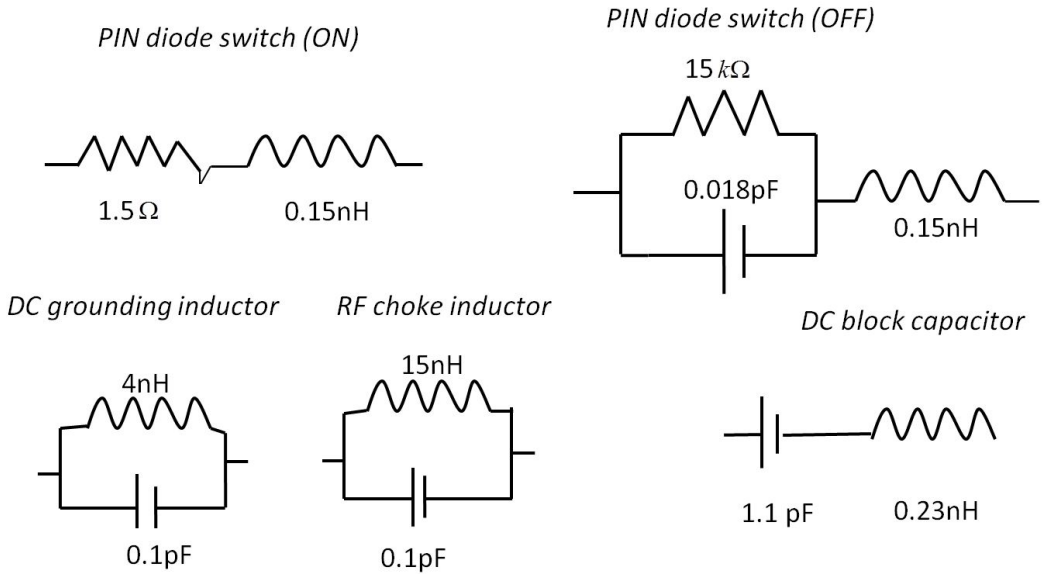

Fig. 2.3: Equivalent circuit models of the lumped components and PIN diode.

Table 2.1: SMD components used in switching circuitry

Component model	Manufacturer	Device	Value	SRF (GHz)
MA4AG910 PIN diode	MACOM	RF switch	NA	NA
LQP03TN 4N0B02D	Murata Electronics	DC grounding inductor	4 nH	5.3
LQP03TN 15NH02D	Murata Electronics	RF chokes inductor	15 nH	5.3
GRM0225C1 H1R1WA03L	Murata Electronics	DC block capacitor	1.1 pF	10

2.2 Working Mechanism

The working mechanism of this MRA is similar to traditional Yagi-Uda array, hence can be explained by following the same principle [30]. The dipole located at the center act as the driven element, while the electrical length of the connected/disconnected pixels, i.e. parasitic elements, of the 3D parasitic layer determines whether they work as directors or reflectors. By changing the states of the interconnecting PIN diode switches between ON and OFF, the electrical length of the parasitic elements can be varied. When the overall electrical length of any connected pixels becomes greater than $\lambda/2$ at the resonant frequency, that portion starts to work as a reflector. For lengths less than $\lambda/2$, the parasitic element works as a director. We note that the transmission and reflection characteristics of 3D parasitic layer can also be thought as that of a meta-surface whose EM impedance changes creating a capacitive or inductive surface depending on the states of interconnecting switches. A meta-surface transmits EM waves at capacitive impedance level while it reflects

them at inductive impedance level, which is illustrated in [31] for the case of a terahertz modulator. For the presented MRA, by connecting and disconnecting various pixels, the amplitude and phase of currents on particular parasitic elements are varied. When the induced currents on the parasitic elements are capacitive and thus in phase with the driven dipole, radiation is enhanced towards that direction; however, when they are inductive and out of phase with the driven dipole, EM wave is reflected from that direction.

This MRA is capable of generating various radiation patterns which can be classified under four cases which are illustrated in Fig. 2.4:

1) *Omni-directional mode*: When all the switches are kept at their OFF state, the individual pixels are electrically short enough to be transparent to the radiated fields of the driven dipole, from which the omni-directional dipole pattern is obtained.

2) *Azimuthal beam-steering modes*: These are similar to patch antenna pattern, where the main beam direction is steered in the azimuth over six different directions corresponding to main beam directions $\phi \in \{30^o, 90^o, \ldots, 330^o\}$. For a given beam-steering direction, the pixels on the surface of rectangular-shaped face to which the beam-steering direction is normal are disconnected while the pixels on the diametrically opposite surface are all connected. The parasitic layer with connected pixels becomes electrically long enough to work as a reflector.

3) *Elevation beam-steering modes*: Similar to the patterns of azimuthal modes, the beam-steering is performed in the elevation plane. The typical beam-steering range is $-18^o < \theta < 18^o$. While for the azimuthal beam-steering, the axis, which runs from the reflector to the director, is in the azimuth plane (x-y plane) and is directed towards the beam-steering direction, for elevation beam-steering this axis is tilted and directed along the direction of elevation beam-steering angle. To this end, the pixel of the top (or bottom) dome is connected to the adjacent first top (or bottom) pixel of the middle part of the parasitic layer to form the director. The reflector is formed by connecting the pixel of the bottom (or top) dome with the adjacent two bottom (or top) pixels, which are located on the diametrically opposite face with respect to the director face. Therefore, the beam can be

steered in both upper and lower elevation planes.

4) *Modified dipole pattern modes (diversity modes)*: This MRA can also generate many other radiation patterns that can be categorized as modified dipole patterns or diversity patterns. Some of these patterns are obtained by combining the interconnecting switch statuses of the above given three cases. For example, if the pixels of face A and B are disconnected to form the directors, while the pixels of the diametrically opposite faces (faces A' and B') are all connected forming the reflectors, the resulting beam steering angle is obtained by the vector sum of azimuthal beam steering directions corresponding to the modes of $A\&A'$ and $B\&B'$. This is shown in Fig. 2.4. As is demonstrated in the system level performance section of the paper, some of these diversity modes are the desired winning modes yielding the best system level performances in terms of throughput and coverage for a given communication scenario.

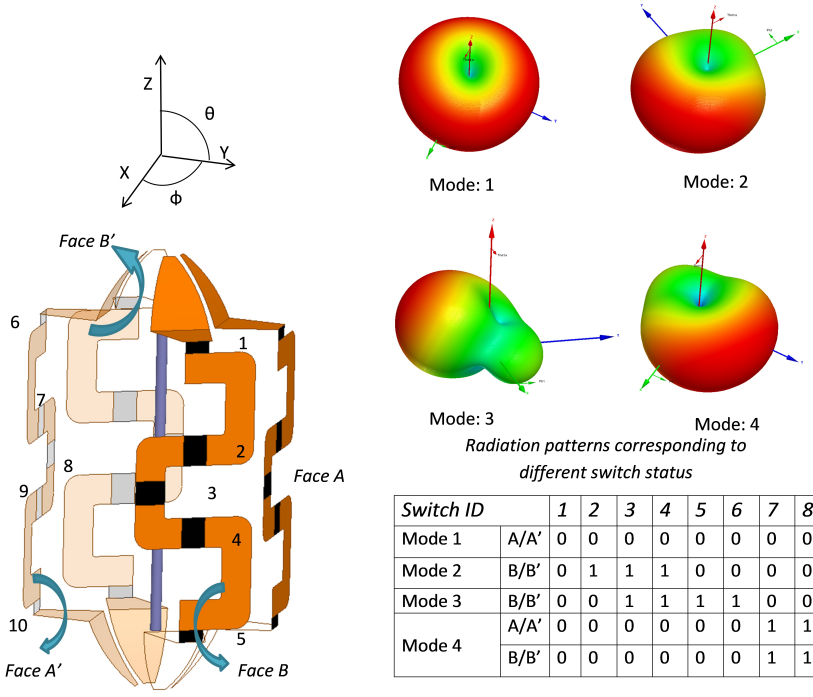

Switch ID		1	2	3	4	5	6	7	8	9	10
Mode 1	A/A'	0	0	0	0	0	0	0	0	0	0
Mode 2	B/B'	0	1	1	1	0	0	0	0	0	0
Mode 3	B/B'	0	0	1	1	1	1	0	0	0	0
Mode 4	A/A'	0	0	0	0	0	0	1	1	1	0
	B/B'	0	0	0	0	0	0	1	1	1	0

'0' indicates OFF state, '1' indicates ON state of the switch

Fig. 2.4: Switch configuration for various modes of operation. For clarity, 4 faces of the hexagonal structure are explicitly depicted. The pixels on the other 2 faces are disconnected.

2.3 Theory of Resonance and Radiation in the Antenna

The interaction between the fed antenna and parasitic layers of the 3D MRA can be illustrated by following transformer principle. EM power is coupled from the primary feed dipole to the secondary 3D parasitic layer. Therefore, neglecting the mutual coupling between parasitic elements of different sides, the equivalent circuit for the 3D MRA for omnidirectional mode of operation can be represented as in Fig. 2.5 below:

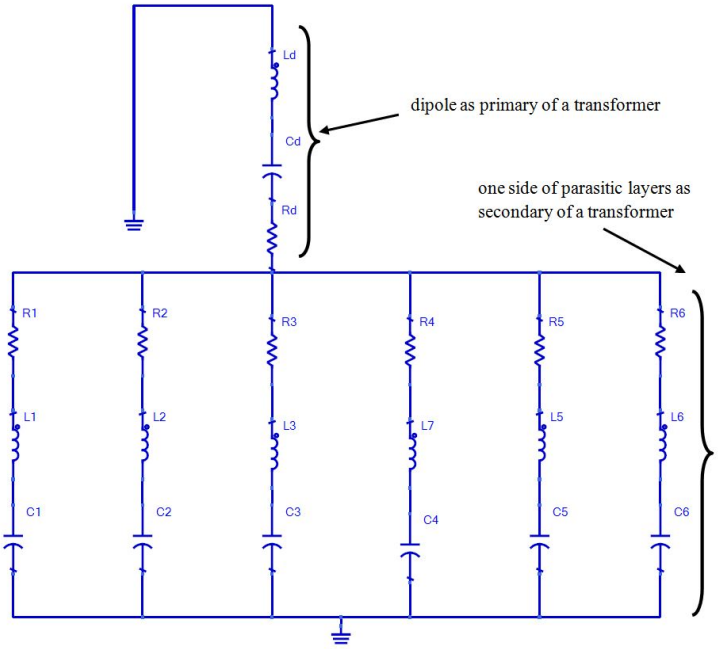

Fig. 2.5: Equivalent circuit model of 3D MRA at omni mode considering switches being perfect short and open.

Input impedance for omni mode can be written as-

$$Z_{in} = Z_d + (Z_1||Z_2||.....||Z_6) \tag{2.1}$$

where $Z_d = R_d + j(wL_d - \frac{1}{wC_d})$, is the lone dipole's impedance and

$$Z_i = R + j(wL - \frac{1}{wC}), i = 1, \ldots, 6,$$

is the impedance of each side of the parasitic pixel layer at omni mode of operation. Since the radiation resistance of these pixels at omni mode is almost negligible, we can take $R \approx 0$

Then after simplifying Eq. 2.1-

$$Z_{in} = Z_d + j(wL_d + \frac{wL}{6} - \frac{1}{wC_d} - \frac{1}{6wC}) \tag{2.2}$$

At resonance, the imaginary part of $Z_{in} \approx 0$, which makes-

$$wL_d + \frac{wL}{6} = \frac{1}{wC_d} + \frac{1}{6wC}.$$

Again, if the feed-gap of the dipole is kept very low, C_d is very high.

So $\frac{1}{C_d} \approx 0$, also $L_d + \frac{L}{6} \approx \frac{L}{6}$

Therefore the resonant frequency in the omni mode can be written as-

$$w = \frac{1}{\sqrt{LC}} \tag{2.3}$$

As it is evident from the above equation that, the resonant frequency of the dipole in case of omni mode is determined by the inductance and capacitance of parasitic pixel layer on each side. For this reason although the lone dipole resonates at around 4.9 GHz, when it is put inside the hexagonal supporting structure containing 3D parasitic layer, it resonates at around 5.2 GHz. In case of any directive mode of operation, the values of L and C in the related branches change. Then based on the values of L_i an C_i (where $i = 1, 2, ...6$) of different sides, a particular surface transmits or reflects EM wave; the fundamental principle behind which has been illustrated in [31]. In general, in order to reflect EM wave at a certain frequency w, for any side-

$$wL_i - \frac{1}{wC_i} > 0 \Rightarrow w > \frac{1}{\sqrt{L_iC_i}} \tag{2.4}$$

Below this cut-off frequency, the electromagnetic surface composed of parasitic pixel

layer and interconnecting switching circuitry begins to transmit EM wave, in the process enabling that portion to work as a director.

The whole 3D MRA, as shown in Fig. 2.5 is remodeled in ADS software considering RF switching circuitry. The diode and other lumped LC components are modeled by following their datasheet (Table 2.1). The parasitic inductance and capacitance of the pixels are optimized as 10 nH and 0.01 pF respectively. Reflection coefficients are compared for omni and azimuth directive modes, which is shown in Fig. 2.6.

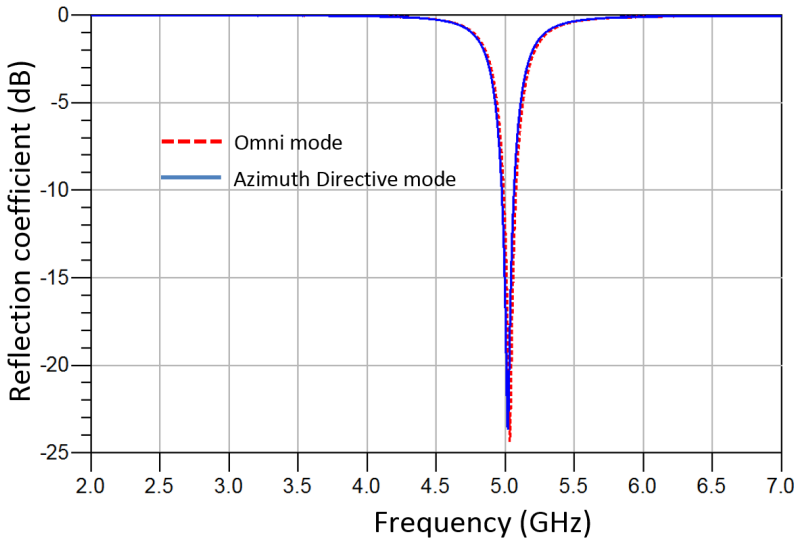

Fig. 2.6: Reflection coefficient comparison of 3D MRA for lumped equivalent model in ADS.

It is evident that- the equivalent circuit model of the 3D MRA also works satisfactorily when the inductance and capacitances of the RF circuitry is taken into consideration.

CHAPTER 3

OPTIMIZATION OF 3D MRA STRUCTURE AND SWITCHING CIRCUITRY

The whole antenna system his optimized in two steps. At first, the 3D parasitic layer's geometry and dimensions have been optimized for perfect short and open switching cases. In this way a design for 3D MRA has been fixed. Later, for the implementation of RF switching in the 3D MRA, lumped components, such as- the values of L, C etc. have been optimized for side and top pixels based on the RF characteristics of MA 907 diode. The whole optimization process will be illustrated step by step in this chapter.

3.1 Optimization of Antenna Geometry and Parasitic Layer

The 3D parasitic pixel layer consists of spiral shaped pixels on sides and conformal inset-domed tetragonal pixels on top and bottom. Satisfactory resonance bandwidth, directive gain, front to back ratio, elevation tilt etc. are taken into consideration during optimization process. During azimuth (ϕ) tilting modes of optimization, proper resonance has been given the utmost importance, making it sure that reflection co-efficient falls well below -10 dB at the resonant frequency with satisfactory impedance bandwidth. However, in case of elevation (θ) tilting modes of optimization, trade off has been made between tilt and resonance bandwidth; since due to asymmetry bandwidth is decreased significantly during these types of modes of operation. Notwithstanding this fact, the logarithmic value of S_{11} was maintained below -10 dB at the resonant frequency for these elevation tilting modes by limiting tilt up to a certain level. The optimization process of the 3D parasitic layer is initiated from the side pixel layer. Later based on that optimized pixel dimension, top and bottom pixel layers are also optimized.

Although directive gain is almost equal for all six symmetric azimuth tilting modes, i.e., $\phi \in \{30^o, 90^o, \ldots, 330^o\}$, however, due to the asymmetry of the modeled dipole near its feed-arms, there is some variation of elevation tilt in different azimuth (ϕ) planes. The

modeled dipole yields maximum elevation uptilt at $\phi = 90^o$ plane while minimum at $\phi = 30^o$ or 210^o plane. So during optimization of gain and tilt of elevation tilting mode, theta uptilt and gain at $\phi = 210^o$ plane has been considered for convenience. For optimizing azimuth mode, 2D gain in $\phi = 30^o$ plane has been taken into account. The optimization process of 3D parasitic layer will be described in the following sub-sections. Subsections 1 to 3 refers to azimuth beam steering mode optimization; while in subsections 4 to 7, elevation beam steering modes' optimization has been described.

3.1.1 Fixing of Pixel Geometry and Optimization of Number of Turns in Spiral Pixel

Initially the project was started with rectangular shaped side pixels, for which a prototype at 2.4 GHz was also fabricated (left-most prototype of Fig. 3.1) having a center to side distance of around $\lambda/4$). However, spiral shaped pixels were preferred later due to some of its advantages, namely- small center to side distance, less number of switches, better resonance performance etc. Several prototypes at 2.4 GHz with spiral turns were also fabricated (second and third prototypes of Fig. 3.1). Later the MRA design was shifted to 5 GHz frequency and the antenna system got smaller eventually.

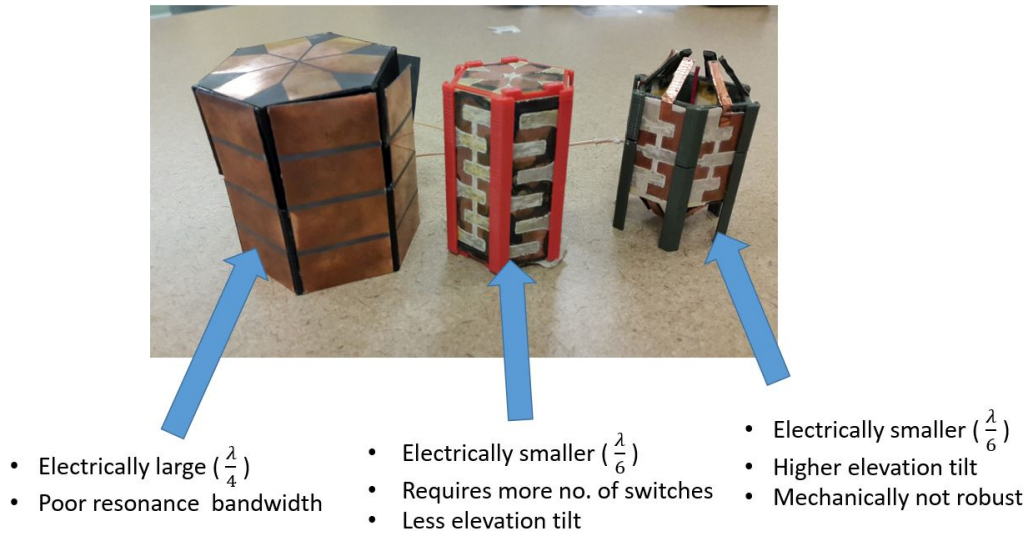

Fig. 3.1: Photo of fabricated prototypes at 2.4 GHz.

The number of turns in spiral pixels plays significant impact on antenna performance. For the number of turns optimization, turns number was varied from 1 (say for a straight pixel) to 5 on a RO4003C substrate having a thickness of 0.5mm, as shown in Fig. 3.2. .

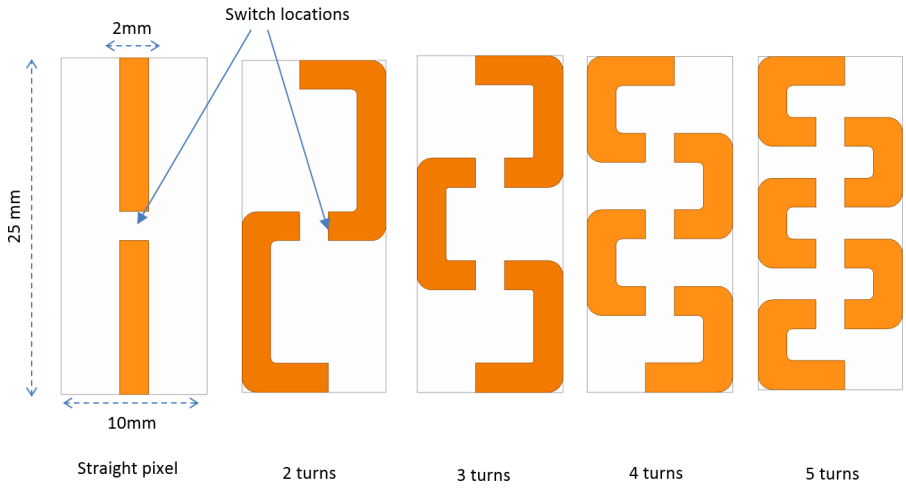

Fig. 3.2: Different number of turns of spiral pixels.

The effects of different turns number are shown in Fig. 3.3. It is evident that with the increase in number of turns although the reflection coefficient improves, but corresponding gain and front-to-back ratio decreases. Since the efficiency of the antenna does not improve that much if the reflection coefficient is decreased far below -10 dB, it is unnecessary to increase the number of turns after a certain point. Besides this, more number of turns require more switches and more complex biasing circuitry; which is also not an efficient approach. As evident from the Table 3.1, satisfactory resonance and radiation properties can be maintained in this structure by keeping turns number to 3 with 2 interconnecting switches at suitable locations. Therefore, optimum number of turns were chosen as 3.

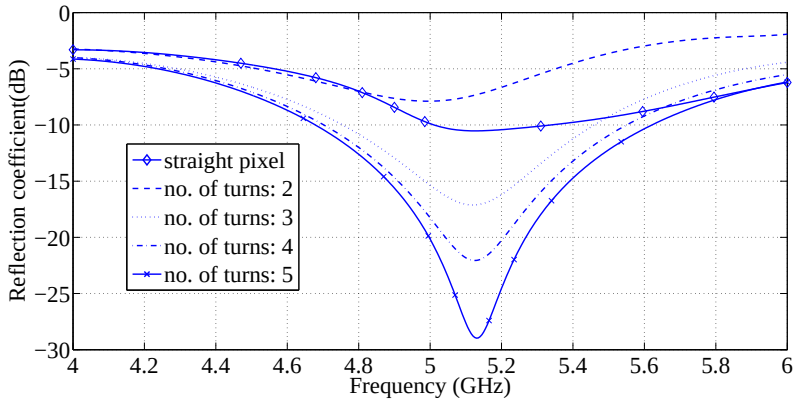

(a)

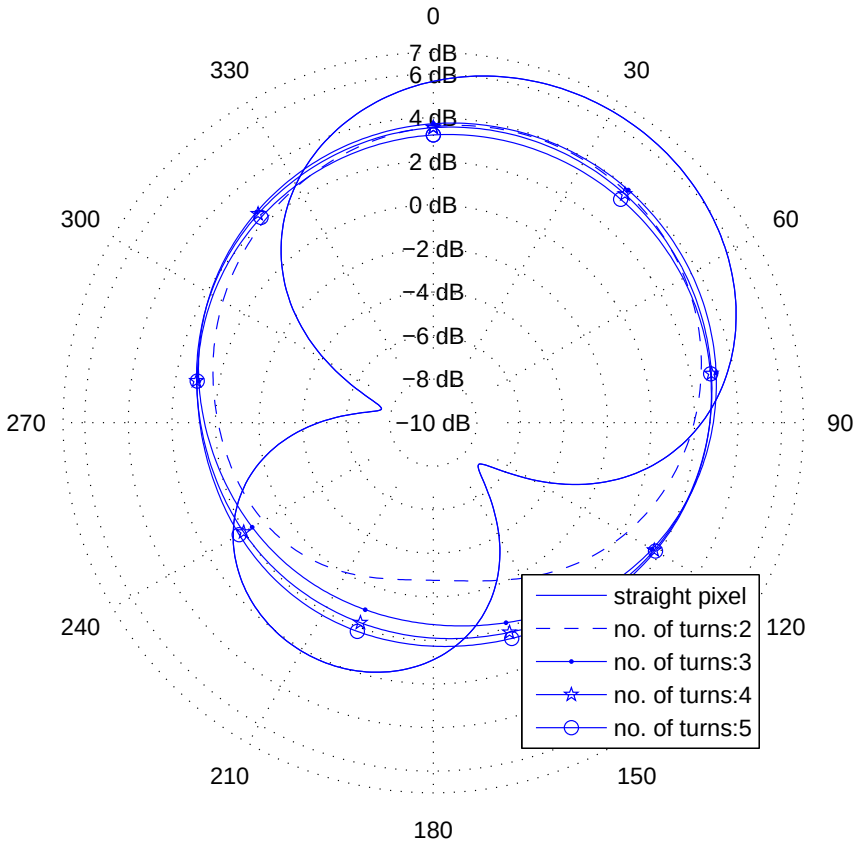

(b)

Fig. 3.3: For different number of turns, comparison of- (a) S_{11}-parameter, (b) 2D gain in azimuth plane at $\theta = 90^o$ at resonant frequencies.

Table 3.1: Gain and front-to-back-ratio comparison (for different number of turns) in the side spiral pixel

Number of turns	Pixel width in mm	Resonant frequency (GHz)	Maximum gain (dB)	Front-to-back ratio (dB)
1(with straight pixel)	2	5.11	6.49	4.38
2	2	5	3.90	4.94
3	2	5.12	3.97	4.79
4	2	5.125	3.74	3.95
5	2	5.135	3.41	3.20

3.1.2 Choosing Number of Switches at Suitable Locations in 3 Turns Pixel

After number of turns optimization, optimum switch locations with different number of switches at symmetric locations are investigated for 3 turns spiral pixel, shown in Fig. 3.4.

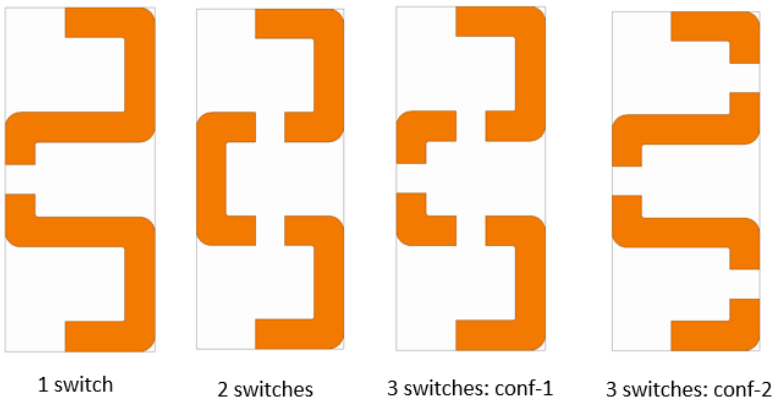

Fig. 3.4: Location of different number of switches in 3 turns of spiral pixel.

It is seen from Fig. 3.5(a) that, less number of switches (only 1 in number) causes problem in resonance when 3 spiral turns is used; whereas with an increased number of switches although resonance improves, front-to-back ratio decreases.

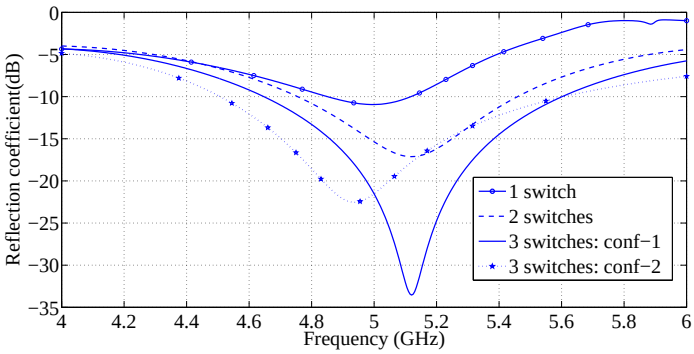

(a)

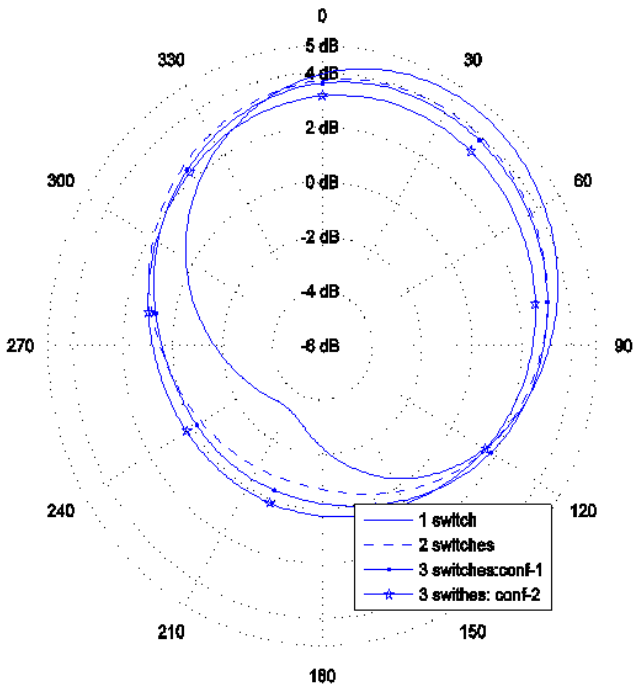

(b)

Fig. 3.5: For different switch locations in 3 turns spiral pixel, comparison of- (a) S_{11}-parameter, (b) 2D gain in azimuth plane at $\theta = 90^o$ at resonant frequencies.

Since during elevation tilting modes of operation, resonance is supposed to worsen even more; it is necessary to maintain quite satisfactory resonance bandwidth for azimuth modes first. Considering all these factors, 3 switches in 3 turn spiral pixel seems to be more practical. However, for 3 switches case,we can have 2 different configurations, shown in Fig. 3.4. 3 switches configuration-1 is chosen finally for several reasons; i) better front-to-back ratio during azimuth mode (as evident from Table 3.2), and ii) more electrical length in its outer segment which can significantly enhance current density on the top and bottom pixel during elevation tilting modes of operation. Therefore, switch configuration-1, i.e., 3 switches at 3 different symmetric locations of the 3 turn spiral pixel were chosen as optimum.

Table 3.2: Gain and front-to-back ratio comparison (for different number of switches) in 3-turn spiral side pixel

Number of switches	Number of turns	Resonant frequency (GHz)	Maximum gain (dB)	Front-to-back ratio (dB)
1	3	5	4.63	7.93
2	3	5.12	3.97	4.79
3(conf-1)	3	5.12	3.85	4.21
3(conf-2)	3	4.94	3.32	3.19

3.1.3 Optimization of Side-pixel Length (PL), width (PW) and its Distance from the Central Dipole(b)

After having the spiral pixel's number of turns and switch locations optimized, other parameters, such as- PL, PW, and b, are optimized. h is fixed at 23 mm symmetric about the dipole center. In Fig. 3.6, these design parameters of the parasitic pixel layers are depicted.

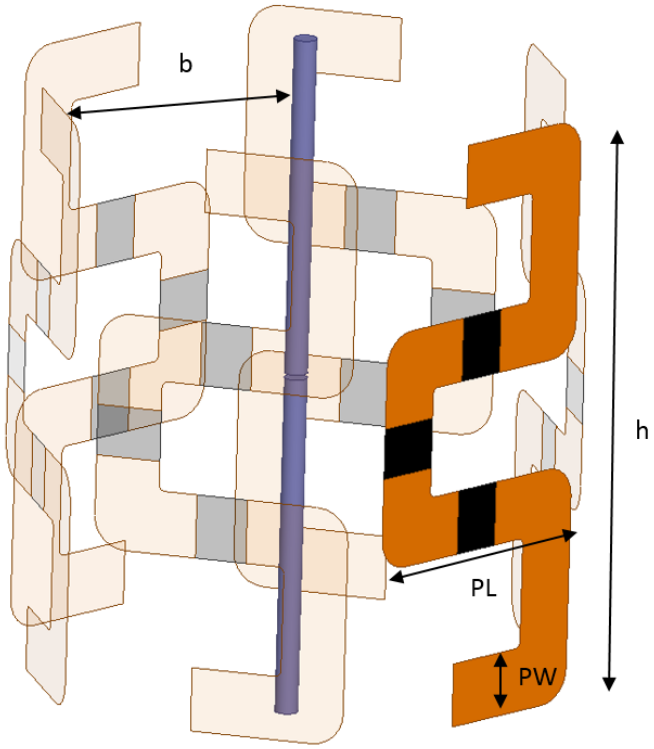

Fig. 3.6: Antenna geometry showing side-pixel length (PL), width (PW) and its distance from the central dipole(b).

In Fig. 3.7, the effect of variation of PL, b, and PW on the impedance bandwidth and azimuthal beam-steering mode radiation pattern is shown. The results are summarized and compared in Table 3.3. It is seen that as b gets smaller, resonance bandwidth, gain and front-to back ratio are improved. It is also seen that with the increase of PW, both gain and front-to-back ratio increase. The jointly optimized dimensions of PL, b, and PW are determined to be 10 mm, 10 mm, and 2.5 mm, respectively.

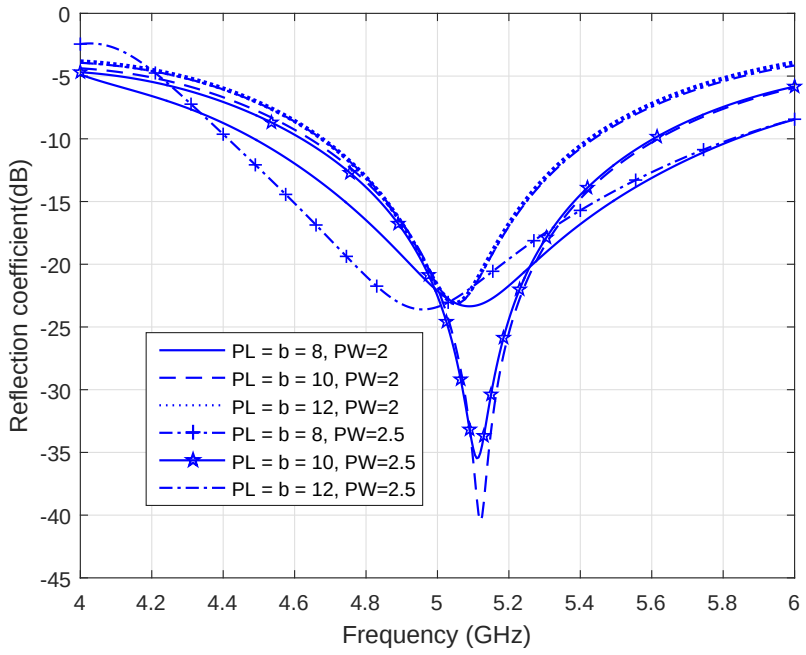

(a)

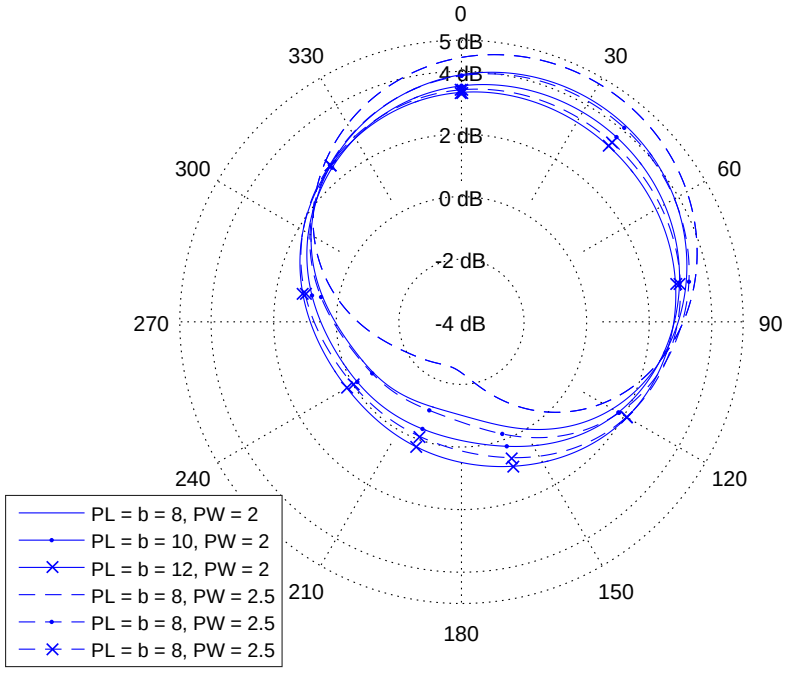

(b)

Fig. 3.7: (a) Reflection coefficient (S_{11}), (b) realized gain in azimuth plane at $\theta = 90^o$ for various PL and b values.

Table 3.3: Impact of PL and b on the realized gain and front-to-back ratio

PL and b in mm	Pixel width (PW) in mm	Resonant frequency (GHz)	Maximum gain (dB)	Front-to-back ratio (dB)
8	2	5.1	4.2	5.3
10	2	5.1	3.7	4.1
12	2	5.1	3.4	3.3
8	2.5	5.0	4.8	7.3
10	2.5	5.1	4.1	5.1
12	2.5	5.1	3.5	3.7

3.1.4 Choosing a Proper Top-bottom Pixel Geometry and Optimization of Inset Distance

The proper design and optimization of top and bottom pixel geometry is important for obtaining elevation or theta tilt and other diversity modes in elevation plane. For the very first prototype at 2.4 GHz shown in earlier Fig. 3.1, pentagonal planar pixels was used. In that case, elevation tilt was a maximum of 10^o degrees. Hence for the purpose of increasing tilt in elevation plane, rectangular slanted pixels were investigated for top and bottom and another prototype was fabricated at 2.4 GHz for the proof of concept. This scheme greatly enhanced theta tilt with a maximum tilt of around 20^o degrees in elevation plane. However, for the placement of switching circuitry, a mechanically more robust structure is necessary. Considering this fact, inset domed shaped pixel on top and bottom was investigated and placed, schematic of which is shown in Fig. 3.8.

The inset domed pixel is composed of two different shapes. On the flatter part, tetragonal pixel having uneven width is placed. For the domed part, conformal tetragonal pixel is used. All the necessary parameters, such as- pixel dimensions at different locations,inset distance, h etc. are optimized one after another to maximize theta tilt which will be described in later subsections of this chapter.

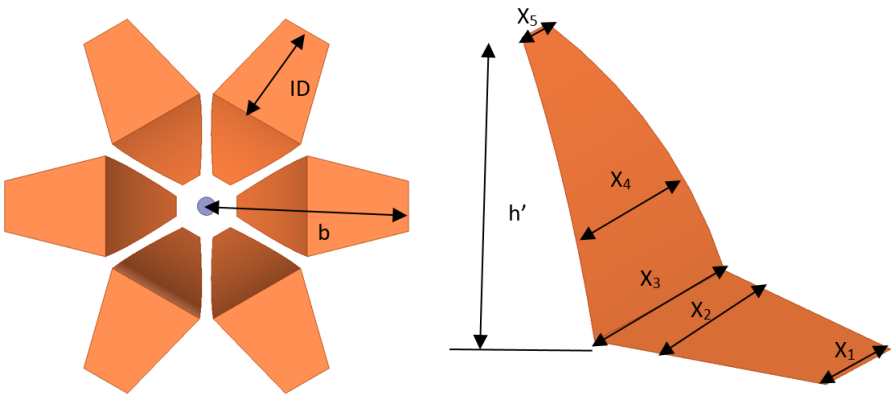

Fig. 3.8: Detailed view and critical design parameters of top and bottom parasitic pixel elements.

Inset distance of the domed part plays significant role in shifting antenna's resonant frequency for the theta tilting modes. It should be noted that- the maximum allowable dimension x_3 of the conformal pixel (shown in Fig. 3.8) also depends on inset distance. At a lower inset distance, wider pixel can be employed; while at a higher inset distance, these dimensions have to be quite smaller so as to arrange them symmetrically on top and bottom of the hexagonal 3D printed supporting structure.

In this section for inset distance optimization, top and bottom conformal pixel dimensions are chosen as: $x_1 = x_3 = x_5$ =2.5 mm, so that inset distance can be varied within a certain range ($3 - 6$ mm) to find its optimum value. As seen from Fig. 3.9(a), with the increase in inset distance, the structure becomes more inductive, thus the resonant frequency shifts towards left. On top of that, with higher inset distance, theta tilt also decreases subtly as evident from Table 3.4. Higher inset distance also needs narrower pixel which negatively affects elevation tilt. Therefore, smaller inset distance with wider pixel is suitable for attaining a better theta tilt. However, we need to maintain a certain inset distance to place the switching circuitry on top and bottom. So an intermediate inset distance of 5 mm is chosen as optimum by trading off little theta tilt for the shake of convenience in RF switching circuitry placement. The antenna performance with respect to various inset

distances is compared in Table 3.4.

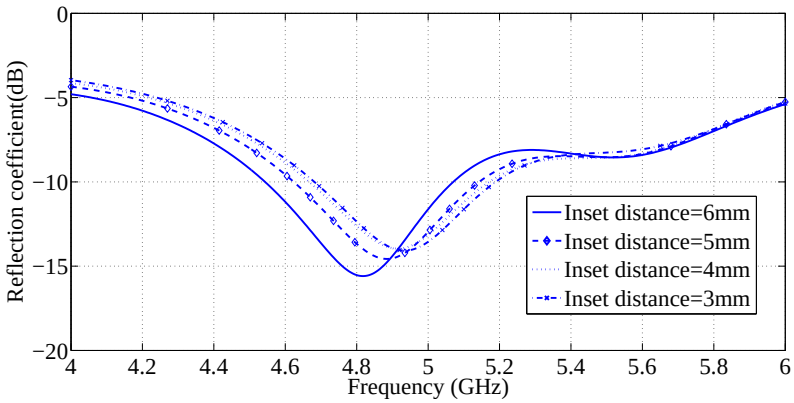

(a)

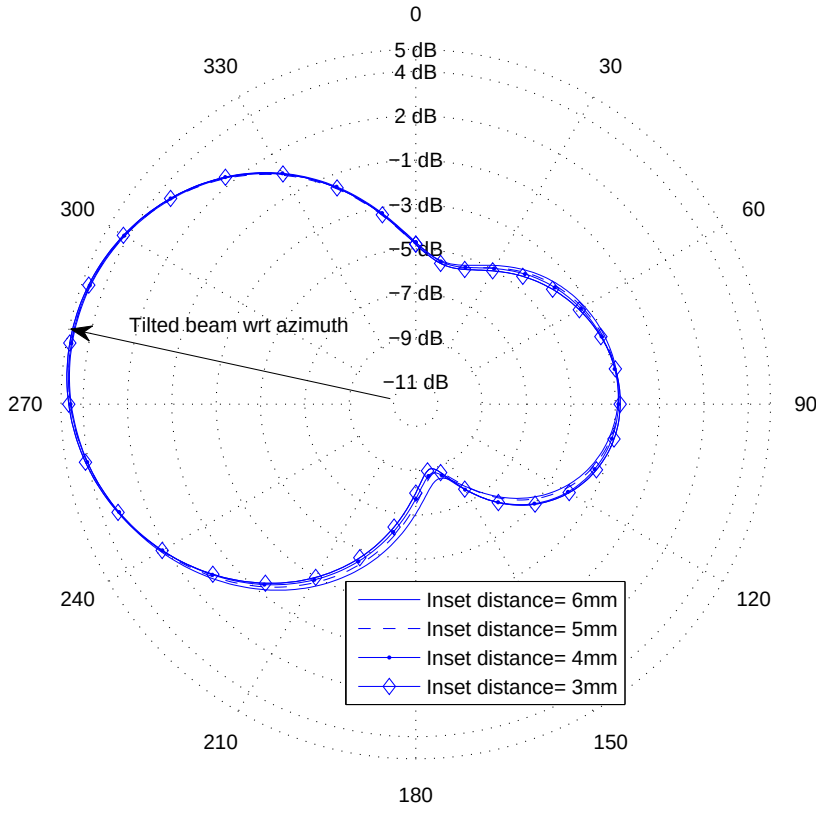

(b)

Fig. 3.9: For different inset distances, comparison of- (a) S_{11}-parameter, (b)2D gain in elevation plane at $\phi = 150^o$ at resonant frequencies.

Table 3.4: Theta tilt and gain comparison (for different inset distance)

Inset distance (mm)	Resonant frequency (GHz)	Theta tilt(^{o}) with respect to azimuth plane	Maximum gain (dB)	Front-to-back ratio (dB)
6	4.82	11	4.74	6.92
5	4.885	11	4.78	6.88
4	4.92	11	4.78	6.83
3	4.95	12	4.85	6.91

3.1.5 Optimization of Top and Bottom Pixel Dimensions

After optimizing the inset distance of the top and bottom conformal pixel(5 mm), its widths at different locations has to be optimized again for maximizing theta tilt. In this optimization, the tilt performance of the antenna due to different values of x_2, x_3 and x_4 is investigated. From Fig. 3.10(b), it is seen that wider pixel provides improved theta tilt by trading off the maximum realized gain very slightly. Comparison is made for the theta tilt and gain performance of the 3D MRA in Table 3.5. It is quite evident that wider pixel shifts the resonant frequency towards left, causes theta tilt to increase. By taking all these factors into account, maximum possible pixel dimensions were chosen as- x_2=5 mm, x_3=5 mm, and x_4= 3.5 mm, which provides 13^o degree theta tilt. This is actually 2^o degree improvement over the last optimized result.

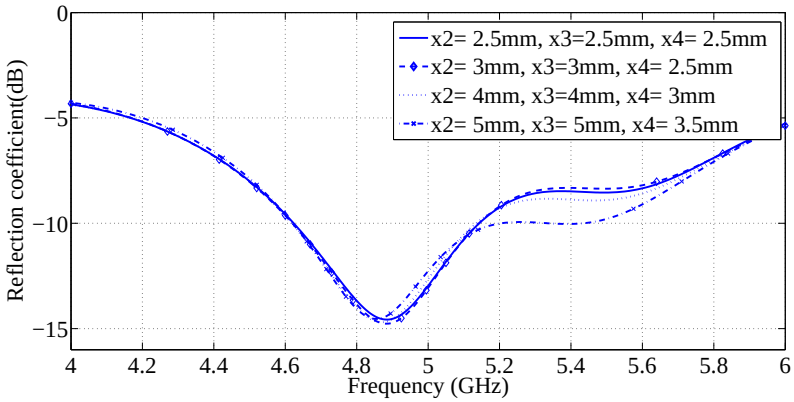

(a)

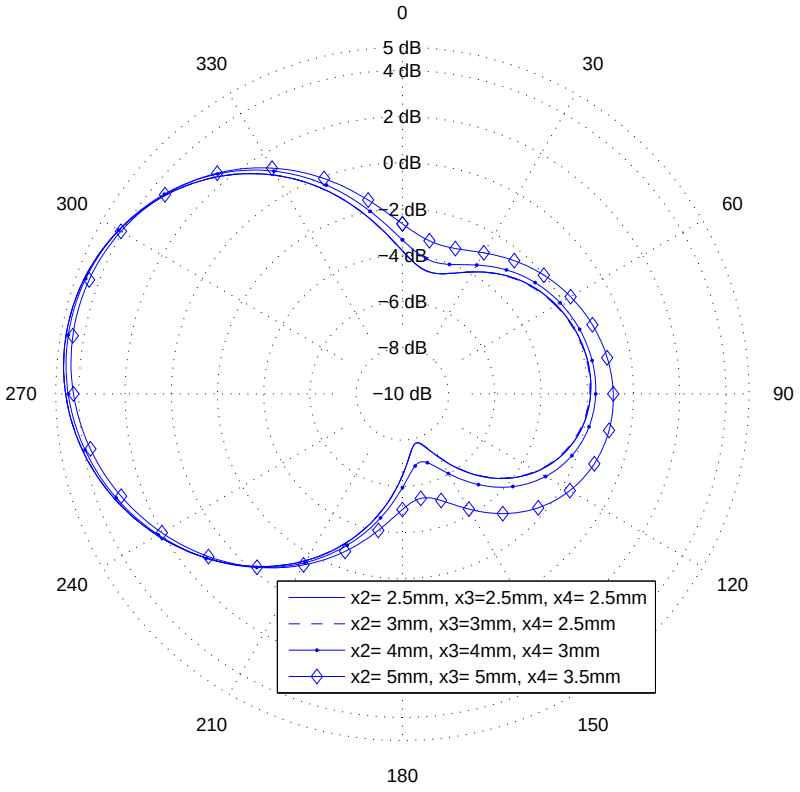

(b)

Fig. 3.10: For different top pixel dimension, comparison of- (a) S_{11}-parameter, (b) 2D gain in elevation plane at $\phi = 150^o$ at resonant frequencies.

Table 3.5: Elevation (θ) tilt, gain and front-to-back ratio comparison (for different pixel width)

Top pixel dimension (mm)	Resonant frequency (GHz)	Theta tilt (^{o} with respect to azimuth plane	Maximum gain (dB)	Front-to-back ratio (dB)
x2=2.5, x3=2.5, x4=2.5	4.885	11	4.78	6.88
x2=3, x3=3, x4=2.5	4.88	11	4.77	6.92
x2=4, x3=4, x4=3	4.865	12	4.69	6.55
x2=5, x3=5, x4=3.5	4.85	13	4.50	5.47

3.1.6 Optimization of Side Pixel Height (h)

The height of the side spiral pixel (h) is shown in Fig. 3.11.

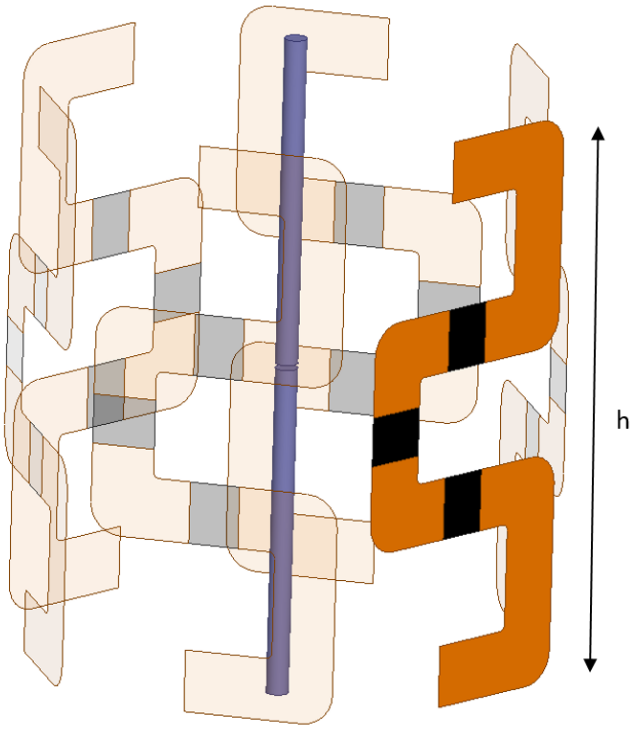

Fig. 3.11: Pixel geometry indicating h.

h has mentionable effect on antenna performance, especially for elevation or theta tilting modes as shown in Fig. 3.12.

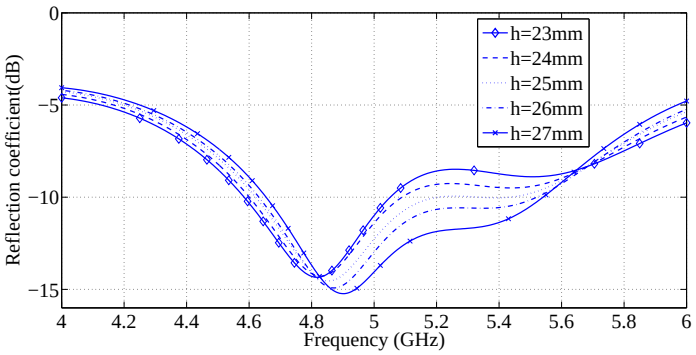

(a)

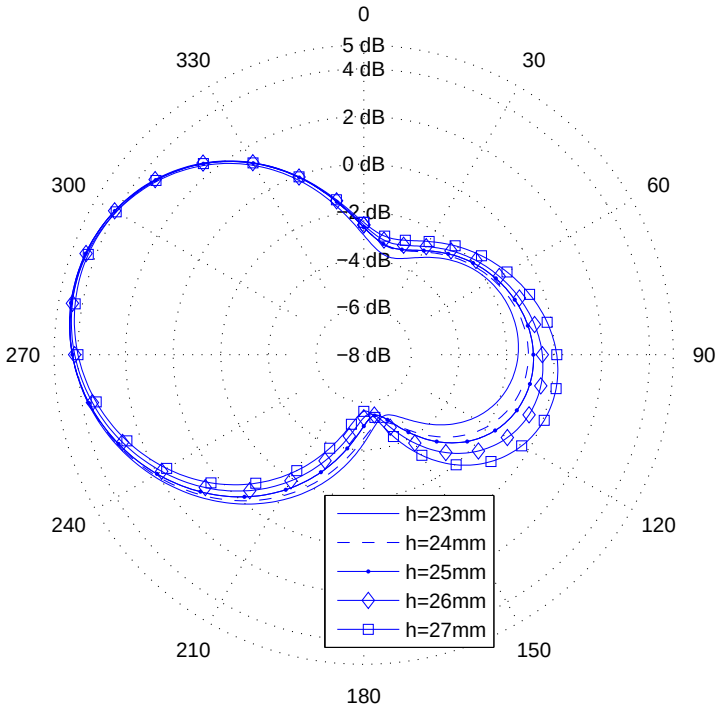

(b)

Fig. 3.12: For different hexagon height (h), comparison of- (a) S_{11}-parameter, (b) 2D gain in elevation plane at $\phi = 30^o$ at resonant frequencies.

Increasing h causes the reflection coefficient and theta tilt to improve gradually. However, front-to-back ratio deteriorates with an increasing h as evident from Table 3.6. Therefore, h is kept at a certain level at 25 mm taking all these factors into account.

Table 3.6: Theta tilt and gain comparison (for different h)

h in mm	Resonant frequency (GHz)	Theta tilt(^{o}) w.r.t. azimuth plane	Maximum gain (dB)	Front-to-back ratio (dB)
23	4.815	13	4.45	6.25
24	4.83	13	4.49	5.73
25	4.85	13	4.50	5.48
26	4.875	14	4.39	4.98
27	4.9	15	4.50	4.34

3.2 Optimization of Lumped Components

After optimizing the antenna geometry, its switching circuitry composed of lumped inductors (L), capacitors (C) etc. are optimized. The lumped components for the side panels have been denoted by- L_{side} and C_{side} respectively, as shown in Fig. 3.13. For the top and bottom parasitic layers, the lumped components are denoted by- L_{top} and C_{top}. In this section, the effects of lumped components on gain, bandwidth and tilting properties of the antenna system will be discussed.

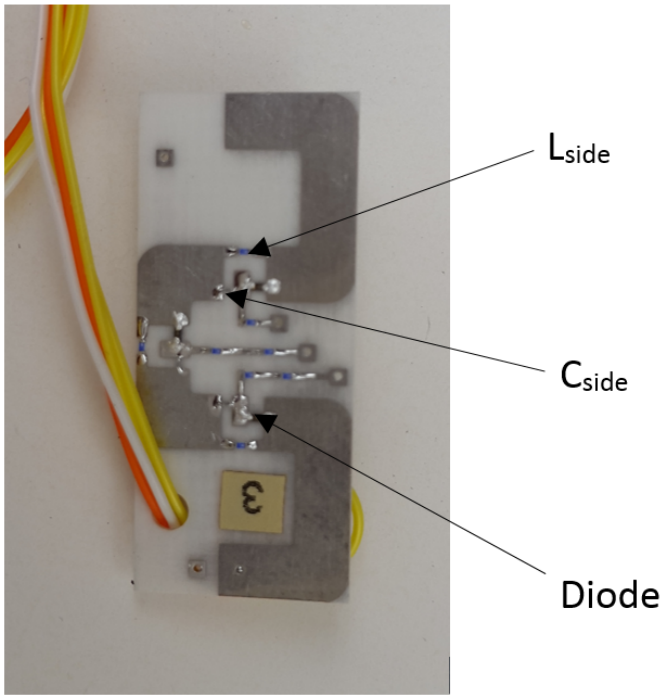

Fig. 3.13: Fabricated pixel structure showing the positions of L_{side} and C_{side} (L_{top} and C_{top} are not shown).

3.2.1 Optimization of Side Panel's DC Block Capacitor (C_{side})

The effect of DC block capacitor (C_{side}) on the gain and tilt of elevation tilting mode is investigated. It is seen from Fig. 3.14(b) that, for very small values of capacitances in between the side pixel segments, the impedance of the connected pixel portion becomes more capacitive; consequently its effect as a reflector diminishes. This in turn, causes that portion to work as a director, which is seen for 0.5 pF and 0.7 pF capacitances. At an intermediate value of C_{side}, i.e., for 1.1 pF, gain and front to back ratio becomes the maximum due to proper resonance. Therefore, we choose the optimum C_{side}= 1.1 pF. The comparison for its different values is explained in Table 3.7. It is mentionable here that other three lumped LC parameters are kept constant as seen from column II of that Table.

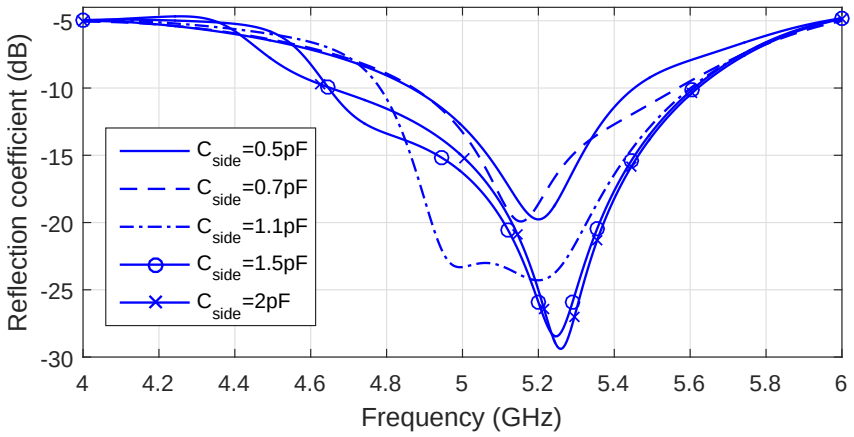

(a)

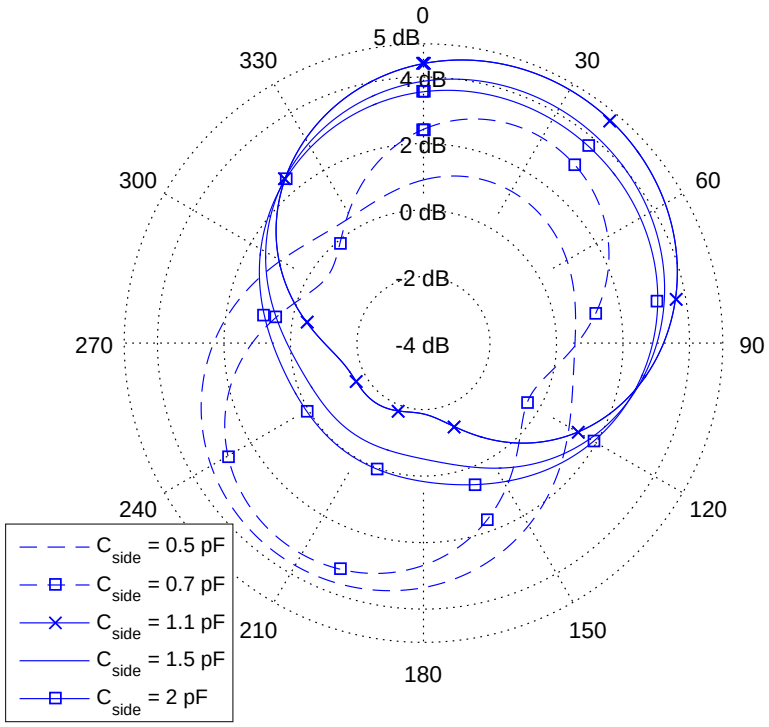

(b)

Fig. 3.14: For different DC block capacitor (C_{side}) on side panels, comparison of- (a) S_{11}-parameter, (b) 2D gain in azimuth plane at $\theta = 90^o$ at resonant frequencies.

Table 3.7: Gain and front to back ratio comparison (for different C_{side})

C_{side} (in pF)	Values of L_{side}, C_{top} and L_{top}	Resonant frequency (GHz)	Maximum gain (dB)	Front-to-back ratio (dB)
0.5	3 nH, 1.1 pF and 2 nH respectively	5.20	3.72 (reflector works as director)	2.44
0.7	same	5.155	3.33 (reflector works as director)	0.2
1.1	same	5.20	4.79	6.53
1.5	same	5.245	4.14	4.72
2	same	5.26	3.76	3.74

3.2.2 Optimization of Side Panel's DC Grounding Inductors (L_{side})

After fixing the optimum value of C_{side}, the value of DC grounding inductor L_{side} between the side pixel segments is optimized. From Fig. 3.15, it is seen that- although bandwidth remains fairly constant, gain and front to back ratio degrades at lower values of L_{side}. However, after increasing L_{side}, gain and front to back ratio does not increase proportionately at some point, as seen from Table 3.8. This effect is however very small, so we choose L_{side}= 4 nH as the optimum inductor value for side panels' switching. This is in the SRF (Self Resonant Frequency) band of the inductor shown in Table 2.1 of Chapter 2.

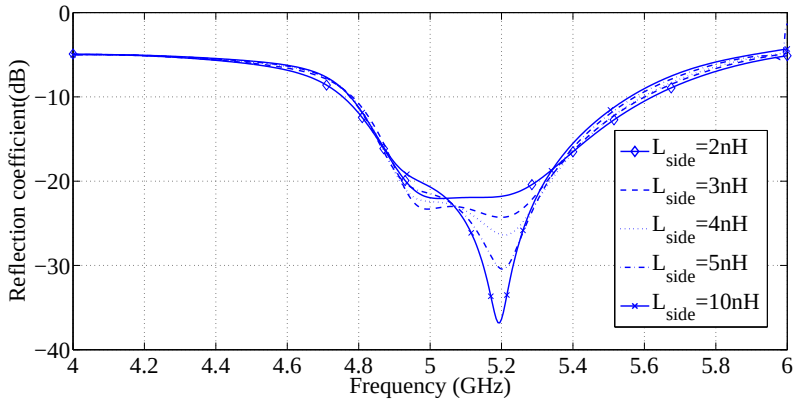

(a)

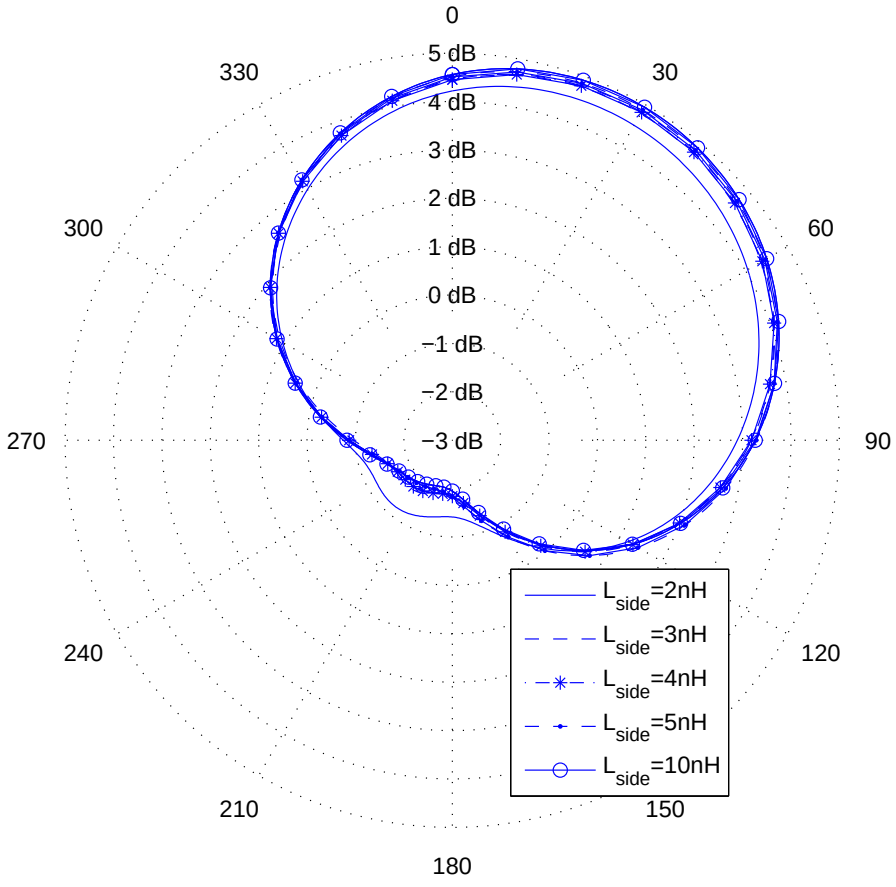

(b)

Fig. 3.15: For different DC grounding inductors (L_{side}) on side panel, comparison of- (a) S_{11}-parameter, (b) 2D gain in azimuth at $\theta = 90^o$ at resonant frequencies.

Table 3.8: Gain and front-to-back ratio comparison (for different L_{side})

L_{side} (nH)	Values of C_{side}, C_{top} and L_{top}	Resonant frequency (GHz)	Maximum gain (dB)	Front-to-back ratio (dB)
2	1.1 pF, 1.1 pF and 2 nH respectively	5.20	4.51	5.75
3	same	5.20	4.79	6.53
4	same	5.20	4.83	6.62
5	same	5.20	4.88	6.77
10	same	5.20	4.95	6.90

3.2.3 Optimization of Top and Bottom Panel's DC Block Capacitors (C_{top})

DC block capacitor (C_{top}) plays significant role in elevation (θ) tilting. As seen from Fig. 3.16(b) and Table 3.9 that- with the increase in capacitance of the top and bottom layer, elevation tilt increases from 7^o to 17^o degree. This is so far the most influential parameter in case of elevation tilt. However, resonant frequency shifts towards the left of 5 GHz band for higher values of C_{top} . Therefore, we need to choose an optimum value of C_{top}= 1.5 pF. It is also hoped that- by using varactors on top and bottom layers, the inter-circuitry capacitances can be varied, which may yield variable elevation tilt for different voltage levels on the varactor terminals. Variable beam tilting ability has certainly many applications in communication systems.

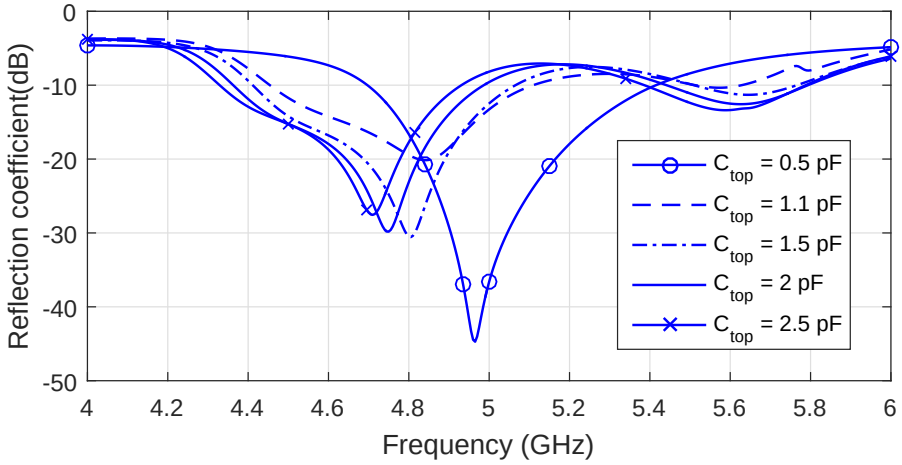

(a)

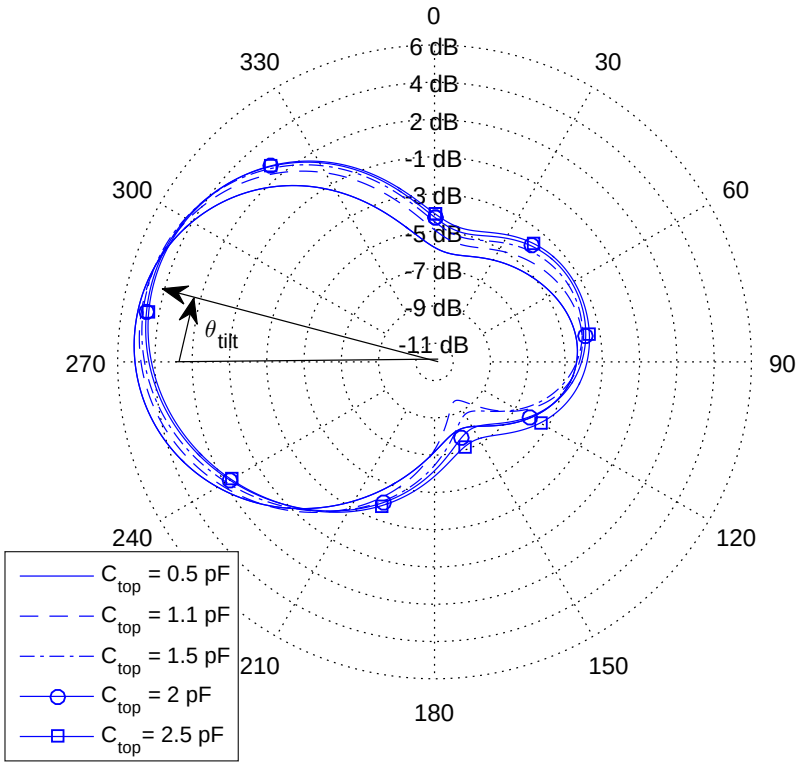

(b)

Fig. 3.16: For different DC block capacitors (C_{top}) on top and bottom panels, comparison of- (a) S_{11}-parameter, (b) 2D gain in elevation plane at $\phi = 30^o$ at resonant frequencies.

Table 3.9: Theta tilt and gain comparison (for different C_{top})

C_{top} in pF	C_{side}, L_{side} and L_{top}	Resonant Frequency (GHz)	Theta tilt w.r.t. azimuth plane	Maximum gain (dB)	Front-to-back ratio (dB)
0.5	1.1 pF, 4 nH and 2 nH respectively	4.965	7	5.17	8.47
1.1	same	4.845	11	4.96	8.81
1.5	same	4.80	14	4.90	9.24
2.0	same	4.75	16	4.75	8.75
2.5	same	4.71	17	4.64	8.21

3.2.4 Optimization of Top and Bottom Panel's DC Grounding Inductors (L_{top})

Apart from C_{top}, the value of DC grounding inductor (L_{top}) impacts resonance and the elevation tilt. It is seen from Fig. 3.17(a) that- for very small value of L_{top}, resonance is completely vanished for the structure. However, with the increase of L_{top}, elevation tilt starts to deteriorate gradually as it is evident from Fig. 3.17(b) and Table 3.10. The optimum inductance value chosen for the top and bottom layer is: 2 nH.

Table 3.10: Theta tilt and gain comparison (for different L_{top})

L_{top} in nH	C_{side}, L_{side} and C_{top}	Resonant frequency (GHz)	Theta tilt (^{o}) with respect to azimuth plane	Maximum gain (dB)	Front-to-back ratio (dB)
0.5	1.1 pF, 4 nH and 1.5 pF respectively	no resonance bandwidth	-	-	-
1	same	4.63	14	1.78	4.63
2	same	4.80	14	4.90	9.24
4	same	4.80	11	4.75	8.18
8	same	4.80	11	4.61	7.71

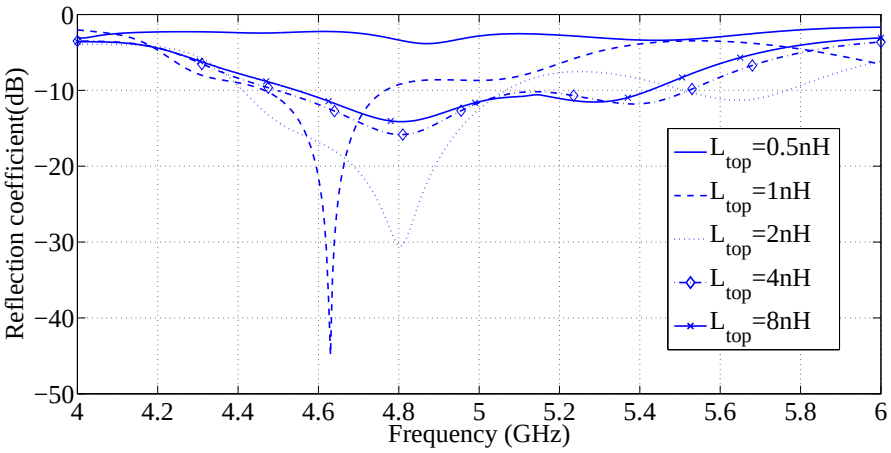

(a)

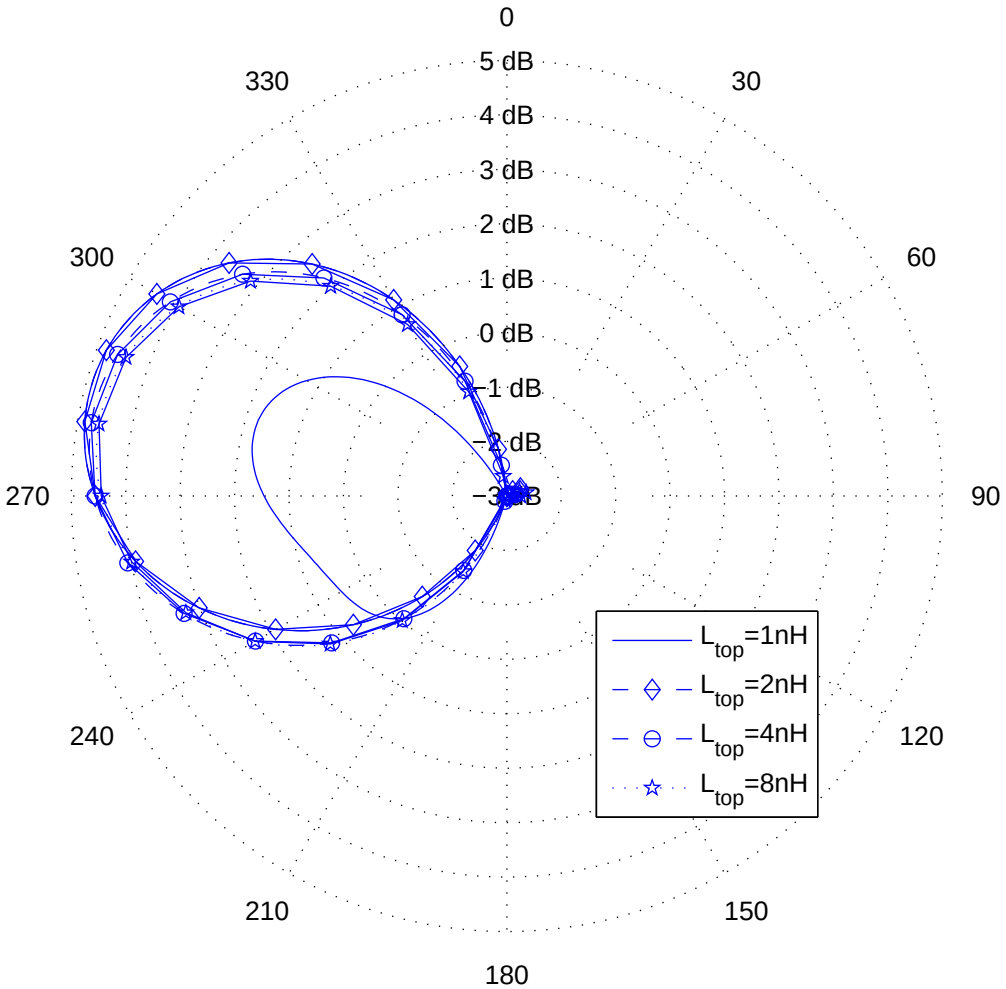

(b)

Fig. 3.17: For different DC grounding inductors (L_{top}) on top and bottom, comparison of- (a) S_{11}-parameter, (b) 2D gain in elevation plane at $\phi = 30^o$ at resonant frequencies.

CHAPTER 4

RESULT COMPARISON OF THE FINAL OPTIMIZED ANTENNA: SIMULATION AND MEASUREMENT

In this section, resonance and radiation characteristics of the final optimized antenna will be discussed and its results will be compared with the fabricated prototype's measurement results. Reflection coefficient or S_{11} parameter of an antenna needs to be investigated first to analyze its resonance characteristics. Once its resonance characteristics are satisfactory, its radiation characteristics (realized gain) are investigated. In this work, all the modes of the fabricated 3D MRA showed good matching in resonance characteristics with their simulation results. However, due to time constraints, it was not possible to measure the radiation patterns of different modes of the 3D MRA.

4.1 Resonance Characteristics

Reflection coefficients are compared between the simulation and fabricated prototypes in Fig. 4.1, where a satisfactory matching has been obtained for omni, azimuth (ϕ) and elevation (θ) tilting modes.

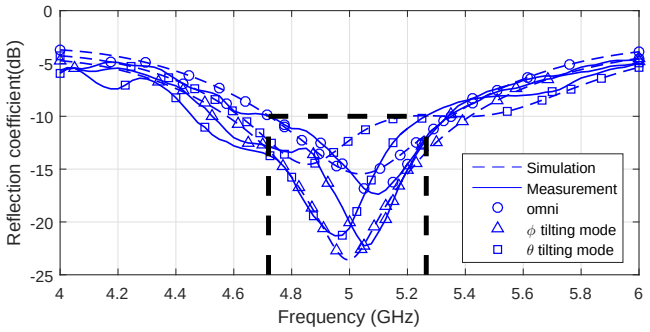

Fig. 4.1: Comparison of the reflection coefficients (S_{11}) from the full-wave analysis and those from the measurements using the prototype having the PIN diode based switching circuitry.

It is seen that- although all the modes show S_{11} bellow -10 dB, ϕ tilting modes have comparatively higher resonance bandwidth. This is because- during ϕ tilting modes of operation, one of the branches of the equivalent circuit in Fig. 2.5, shown in chapter 2, will have very high inductance value; this in turn mitigates the effects of other capacitive elements. The result is low quality factor and high impedance bandwidth at resonance near 5 GHz. It is also seen that- starting from omni to θ tilting mode, the resonance frequency shifts towards left since the antenna becomes more inductive with the closing of more number of switches in the parasitic layer.

4.2 Radiation Characteristics

2D gain plot for different directive azimuth beam steering modes are shown in Fig. 4.2.

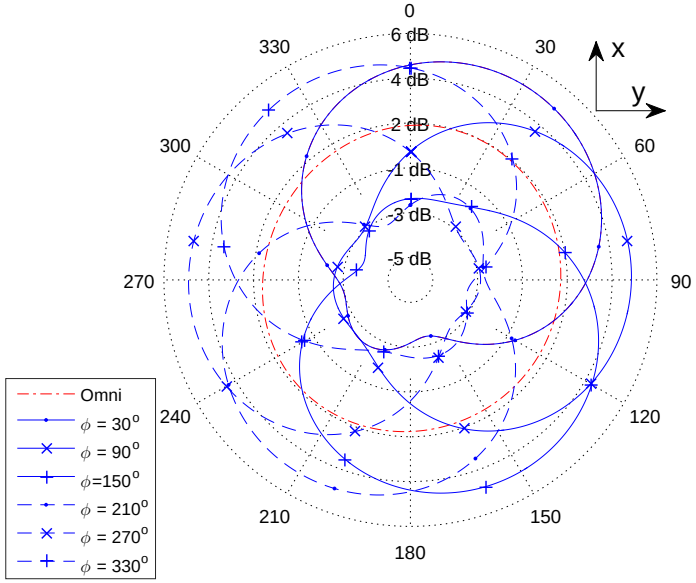

Fig. 4.2: Realized gain pattern for the optimized MRA at 5 GHz, for omni-mode and different azimuth steering modes at (x, y)-plane ($\theta = 90^o$) with beam steering towards $\phi \in \{30^o, 90^o, \ldots, 330^o\}$.

It is seen from Fig. 4.2 that- when one reflector at opposite face is used, a maximum

directive gain of around 4.9 dB is obtained at each 60^o interval in phi plane. Noticeable fact here is the improvement of directive gain from 4.1 dB to 4.9 dB due to using PIN diode switch instead of earlier perfect open and short switch. Although PIN diode has some insertion loss, this sudden increase in gain happens due to series resonance of diode inductor at ON state with adjoining DC block capacitor.

From Fig. 4.3, we see that for the elevation tilting mode, a maximum tilt of 29^o is obtained. Down-tilt in $\phi = 270^o$ plane is comparatively less due to the effect of coaxial cable on that side. Asymmetry in the modeled dipole's arm is another reason for the variation of elevation or theta tilt in different azimuth or phi planes.

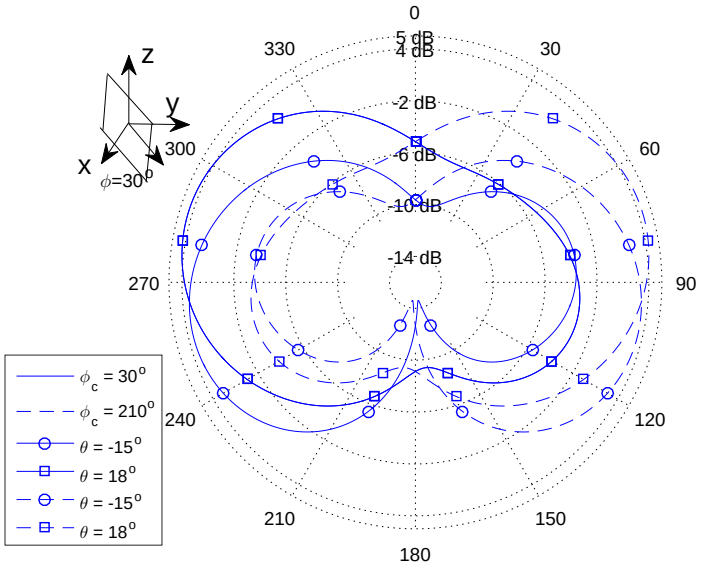

Fig. 4.3: Realized gain pattern for the optimized MRA at 5 GHz, for different elevation tilting modes at $\phi = 30^o$ and $\phi = 210^o$ planes.

Apart from conventional phi and theta tilting modes, this 3D MRA is also capable of producing different diversity patterns shown in Fig. 4.4.

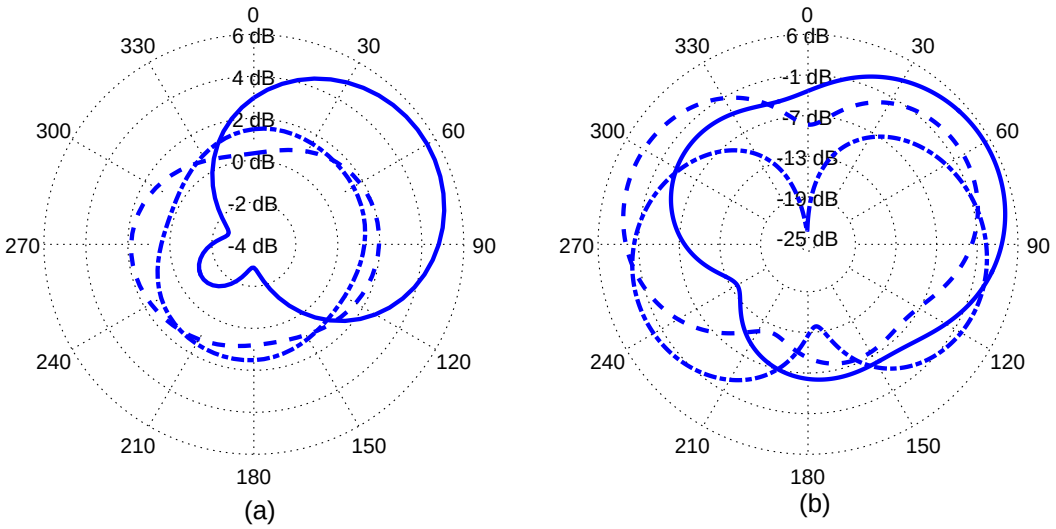

Fig. 4.4: For the optimized antenna- (a) Azimuth diversity modes at $\theta = 90^o$ plane, (solid: azimuth mode with 2 adjacent reflectors dash: dash-dot: (b) Elevation diversity modes at $\phi = -30^o$ plane at resonant frequencies, solid: dash: dash-dot:

For directive antennas, it is necessary to yield a constant gain over the operating frequency band. Hence frequency vs. realized gain is also investigated for the azimuth beam steering mode of the antenna, which is shown in Fig. 4.5.

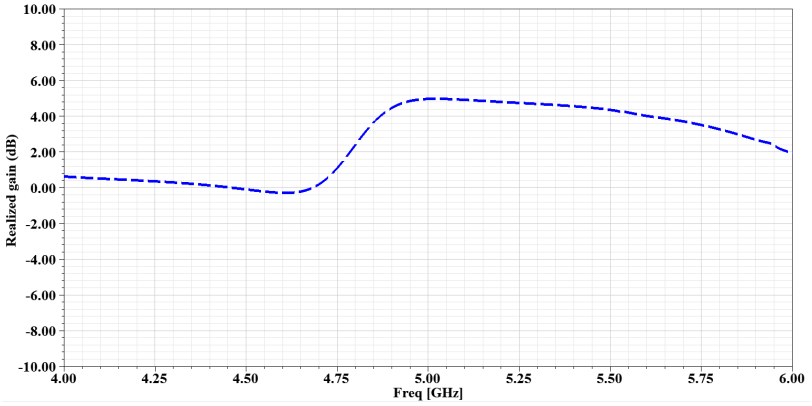

(a)

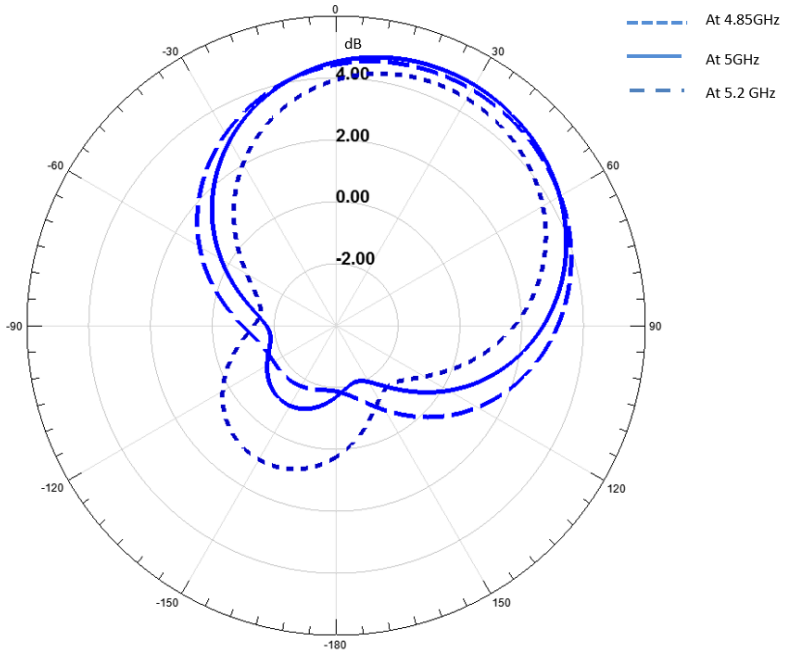

(b)

Fig. 4.5: (a) Realized gain vs. frequency plot, (b) Realized gain for different frequencies at azimuth plane at $\theta = 90^o$.

It is seen that- in the frequency range $4.85 - 5.65$ GHz, the antenna shows realized gain in the range of $4 - 5$ dB, which is quite satisfactory. Also it shows greater gain at 5 GHz than any other frequency in the band.

CHAPTER 5

RADIATION PATTERN MRA FOR WIRELESS HETEROGENOUS NETWORK

We next investigate the performance of the parasitic MRA in a 5G heterogenous wireless network [32]. With 3D pattern reconfigurability, this antenna provides great flexibility in adjusting the signal-to-interference plus noise ratio (SINR) distribution over the desired coverage area.

5.1 System Model

We consider a heterogenous network (HetNet) of K base stations (eNBs), each of which has S sectors and L femto cell access points (FAPs) [33,34]. Let $\mathcal{B} = \{B_{s+(k-1)S}, k = 1,\ldots,K, s = 1,\ldots,S\}$ and $\mathcal{F} = \{F_l, l = 1,\ldots,L\}$, denote the set of all eNB sectors and FAPs, respectively. User-i, U_i, $i \in \mathcal{U} \triangleq \{1,\ldots,U\}$ may be served by one of the eNB sectors or FAPs. We will look into the details of serving cell selection later. Let $X_j \in \mathcal{X} \triangleq \{\mathcal{B} \cup \mathcal{F}\}$ denote the serving station for U_i. Furthermore, let $\mathcal{U}_j = \{j_1,\ldots,j_{|\mathcal{U}_j|}\} \subseteq \mathcal{U}$ denote the set indices of the users being served by X_j. In the following, we refer to a UE served by and eNB and FAP as Macro-UE and Femto-UE, respectively.

Our focus in this work is an ultra dense femto cell deployment scenario for which $L \gg K$. It is assumed that the antenna radiation pattern at B_k can be selected from M_B different options, but it is fixed once it is selected. On the other hand, each FAP is equipped with the MRA antenna element with M_F modes of operation that can dynamically be switched. Each user is assumed to have omni-directional antennas. Let us denote the complex e-field radiation patterns at B_k, F_l and U_i by $\vec{B}_j(\theta,\phi;\nu)$, $\vec{A}_l(\theta,\phi;\mu)$, and $\vec{G}_i(\theta,\phi)$, respectively, where $\nu \in \mathcal{M}_B \triangleq \{1,\ldots,M_B\}$ for B_j, and $\mu \in \mathcal{M}_F \triangleq \{1,\ldots,M_F\}$ for F_l, denotes the indices of the selected antenna pattern at B_j, and the MRA excited mode at F_l, respectively. Here, $\vec{A}(\theta,\phi) = A_\theta(\theta,\phi)\hat{\theta} + A_\phi(\theta,\phi)\hat{\phi} \triangleq [A_\theta(\theta,\phi)\ A_\phi(\theta,\phi)]^T$ denote the e-field pattern in spherical coordinates.

Let us model the wireless channel from transmit station X_j to receiver U_i via a double-directional multi-path prorogation mechanism [35,36]. Assuming narrow band transmission, the channel gain at time t and frequency f can be expressed as

$$h_{i,j}(t,f;\eta_j) = \sum_{p=1}^{P} c_{i,j}\langle \vec{G}_i(\Psi_p), T_p\vec{X}_j(\Omega_p;\eta_j)\rangle e^{j2\pi v_p t - f\tau_p} \tag{5.1}$$

where T_p is the 2×2 matrix representing the polarization leakage between the orthogonal polarization components of the E-field radiation, $\Psi_p = (\vartheta_p, \varphi_p)$ and $\Omega_p = (\theta_p, \phi_p)$ denote the angle of arrival and angle-of-departure, respectively, for the p^{th} path, and

$$\vec{X}_j(\Omega_p;\eta_j) = \begin{cases} \vec{B}_j(\Omega_p;\nu_j) & 1 \le j \le KS \\ \vec{A}_{j-KS}(\Omega_p;\mu_{j-KS}) & KS+1 \le j \le KS+L. \end{cases} \tag{5.2}$$

The notation $\langle \vec{a}, \vec{b}\rangle = a_\theta^* b_\theta + a_\phi^* b_\phi$ denotes the inner product. We note that $j \in \{KS+1,\ldots,KS+L\}$ indicates that the transmitter is F_{j-KS}, the channel gain depends on the antenna mode, μ_l at that F_l with $l = j - KS$. For ease of notation, we drop (t,f) and use $h_{i,j}(\eta)$ to emphasize the dependance of underlying antenna to the channel gain with η denoting the MRA mode of eNB or FAP. Furthermore, since the eNB sector antennas are fixed by initial design, that is, $\boldsymbol{\nu} = (\nu_1,\ldots,\nu_{KS})$ is fixed, the only variation in antenna mode state of whole network is due to the antenna modes at FAPs, $\boldsymbol{\mu} = (\mu_1,\ldots,\mu_L)$.

The average signal-to-interference plus noise ratio (SINR) at U_i being served by X_i is given by [37]

$$\rho_i(\boldsymbol{\mu}) = \frac{P_i g_{i,i}(\eta_i)}{\sum_{j\neq i} P_j g_{i,j}(\eta_j) + \sigma^2} \tag{5.3}$$

where $g_{i,j}(\eta_j) = E(|h_{i,j}(t,f;\eta_j)|^2)$ is the long-term channel power between U_i and X_j. The achievable rate at U_i is then $R_i(\boldsymbol{\mu}) = \log(1+\rho_i(\boldsymbol{\mu}))$. For a bandwidth of W_i Hz allocated to U_i, we defined the average throughput per UE as $\Gamma_i = W_i R_i(\boldsymbol{\mu})$. Note that the Γ_i, $i = 1,\ldots,U$ can be imagined as samples from a random distribution. With this view, the α-percentile coverage is defined as the throughput Γ_α such that $\Pr(\Gamma \le \Gamma_\alpha) = \alpha$. Γ_α is an

important system performance metric as it indicates the smallest average throughput that $U(1-\alpha)$ users out of U users in the network can achieve.

5.2 RA Mode Optimization

We can define various network utility functions to assess the over all system performance. In this work, we study the impact of MRAs on the capacity and coverage performance. To that end, let W be the total available bandwidth at each station X_j, and let $W_{j,i}$ denote the bandwidth allocated for U_{j_i}. To be fair, we set equal bandwidth allocation among users at each X_j, that is, $W_{j,i} = W/|\mathcal{U}_j|$. We consider proportional fairness (PF) utility for emphasizing coverage and capacity performance of the network [38]. The PF utility can be expressed as

$$\Upsilon(\boldsymbol{\mu}) = \sum_{j=1}^{KS+L} \sum_{i \in \mathcal{U}_j} \log\left(\frac{W}{|\mathcal{U}_j|} R_i(\boldsymbol{\mu})\right). \tag{5.4}$$

Hence, the goal is to determine MRA modes $\boldsymbol{\mu}$ for which the network utility in (5.4) is maximized:

$$\boldsymbol{\mu}^* = \underset{\boldsymbol{\mu}}{\operatorname{argmax}}\, \Upsilon(\boldsymbol{\mu}). \tag{5.5}$$

The problem in (5.5) is a combinatorial problem and L^{M_F} different options exist for the FAPs in the network; therefore, a brute-force approach will be formidable when L or M_F is large.

If a central processing entity is provided with the signal quality information from all users, a centralized approach can be sought. This approach requires extensive message exchanges. Alternatively, this overhead can be avoided by performing mode selection locally at each FAP. To that end, we propose a distributed mode selection scheme where each FAP optimizes its MRA mode based only on locally obtained signal measurements.

5.2.1 Distributed Mode Selection

Assume that each access point collects the signal quality measurements from nearby users. For example, in 3GPP LTE-A, reference signal received power (RSRP) is evaluated at the users and fed back to the associated access station [39]. Let $\mathcal{V}_j$ denote the set of users whose signal measurements are available at access station-j. Using (5.4), the estimated utility can then be written as

$$\hat{\Upsilon}(\boldsymbol{\mu}) = \sum_{j=1}^{KS} \hat{\Upsilon}_j(\boldsymbol{\mu}) + \sum_{l=1}^{L} \hat{\Upsilon}_l(\boldsymbol{\mu}) \tag{5.6}$$

with

$$\hat{\Upsilon}_j(\boldsymbol{\mu}) = \sum_{i \in \mathcal{V}_j} \log\left(\frac{W}{|\mathcal{V}_j|} R_i(\boldsymbol{\mu})\right) \tag{5.7}$$

representing the local utility at the access station-j. The first summation in (5.6) is due to the UEs served by eNBs. The variations on MRA modes of FAPs may create variations on the UE's served by eNBs; however, due to the relatively smaller transmit power levels and lower antenna gains at FAPs, the impact is not severe. Thus, in this work, we ignore the impact of FAP MRA mode optimization on Macro-UEs and focus the maximization of second summation in (5.6). Using Jensen's inequality, we can write an upper bound on the expected utility $\hat{\Upsilon}_l(\boldsymbol{\mu})$ as

$$E\{\hat{\Upsilon}_l(\boldsymbol{\mu})\} \leq \sum_{i \in \mathcal{V}_l} \log\left(\frac{W}{|\mathcal{V}_l|} E\left\{R_i(\boldsymbol{\mu})\right\}\right). \tag{5.8}$$

Substituting (5.3) in (5.8) and applying Jensen's inequality again, we obtain

$$E\{\hat{\Upsilon}_l(\boldsymbol{\mu})\} \leq \sum_{i \in \mathcal{V}_l} \log\left(\frac{W}{|\mathcal{V}_l|} \log\left(1 + \frac{P_i g_{i,l}(\mu_l)}{\sum_{j \neq l} P_j g_{i,j}(\eta_j) + \sigma^2}\right)\right). \tag{5.9}$$

The summation in the denumerator of (5.9) is the aggregated interference from all access points onto user-$i \in \mathcal{V}_l$. eNBs have antennas with a fixed radiation pattern, and therefore,

the aggregate interference from eNBs do not vary significantly. On the other hand, the interference from FAPs to the UEs served by other FAPs may vary for different MRA modes, especially in case of ultra-dense small cell deployment. Since no feedback message is available regarding the mode selection at other FAPs, we assume that the aggregate interference in (5.9) is fixed for mode selection purposes. Under these assumptions, the MRA mode optimization at F_l can be approximated as

$$\mu_l^* = \underset{\mu_l}{\operatorname{argmax}} \sum_{i \in \mathcal{V}_l} \log\log\left(1 + \frac{P_i g_{i,l}(\mu_l)}{I_0 + \sigma^2}\right) + |\mathcal{V}_l| \log W - |\mathcal{V}_l| \log |\mathcal{V}_l| \tag{5.10}$$

where I_0 denotes the aggregate interference level over thermal noise density. The optimization in (5.10) has significantly lower complexity than the one in (5.5) since (5.10) requires mode optimization for only a single FAP and over the UEs in the vicinity of this FAP.

5.2.2 Cell Selection and Mode Optimization

Since the average received signal quality (e.g., RSRP) at the UEs for different MRA modes may differ from one mode to another, cell selection has to be taken into account during mode selection [40]. Here, we consider biased cell selection [41] where the serving cell j^* is decided using

$$j^* = \underset{j}{\operatorname{argmax}}\, \delta_j P_j g_{i,j}(\eta_j) \tag{5.11}$$

with δ_j denoting the bias towards access station-j. In this case, some of the UEs appearing in the measurement list $\mathcal{V}_l$ of F_l may end up being served by another station due to the bias δ_j and the selected antenna mode at access station-j if it is a FAP. Thus, the antenna mode selected at F_l under the assumption that all UEs in $\mathcal{V}_l$ would be served by this FAP may create significant interference to the UEs which are actually served by nearby access point. To combat this issue, one could extend the optimization in (5.10) over all non-empty subsets of $\mathcal{V}_l$. Here, we provide a low-complexity alternative solution to the exhaustive

search approach. To that end, for each mode, let us sort the users in measurement list $\mathcal{V}_l$ in descending order according to the received signal qualities. Let $\{i_1, \ldots, i_{|\mathcal{V}_l|}\}$ indicate the UEs in the sorted set, with i_1 denoting the highest signal quality, and i_2 the second one, and so on. The joint optimization of MRA modes along with the candidate served UEs can then be expressed as

$$\mu_l^* = \underset{\mu_l}{\operatorname{argmax}} \max_{J} \sum_{j=1}^{J} \log\log\left(1 + \frac{P_{i_j} g_{i_j,l}(\mu_l)}{I_0 + \sigma^2}\right) + J \log W - J \log J. \tag{5.12}$$

Hence, the MRA mode at F_l is selected such that those UEs in $\mathcal{V}_l$ contribute more to the local utility than the UEs receiving lower signal quality from this FAP, and thus avoid the off-loading of those UEs to the FAP for which the MRA mode optimization do not get utility improvement. We note that W in optimization (5.12) can be taken in units of the shared resources. For example, in 3GPP LTE-A, the minimum scheduling unit is one resource block (RB), a slot of 180 kHz wide in frequency and 0.5 ms duration in time, and for a 10 MHz bandwidth, 50 RBs exist, thus $W = 50$ RBs [39].

5.3 Simulations

Let us next investigate the performance of the parasitic MRA and associated mode selection scheme in a wireless heterogenous cellular network. We consider a $S = 3$-sector, and $K = 19$ eNBs, totalling to 57 base stations. We assume a hexagonal grid based deployment and a wrap-around technique described in [42] to ensure accurate modelling of inter- and intra-cell interference. UEs are deployed according to the hot-spot scenario where a fraction of UEs are uniformly randomly dropped within a number of clusters that are also uniformly randomly created in the 57-cell area. Two FAP deployment scenarios are studied: (i) Random deployment where FAPs are randomly dropped across the 57-cell area, and (ii) Planned deployment where FAPs are dropped randomly within 50 metres of the UE clusters. We employ the spatial channel model described by 3GPP in [36, 43] targeted for

performance evaluation of 5G networks. This channel model assumes a double directional MIMO multi-path channel and takes into account the antenna radiation patterns. We extended this channel to the case of MRAs that can assume multiple modes of operation with different radiation patterns. The 3D radiation patterns are obtained from full-wave analysis for various modes of operation as described in Chapter 3 (see for example, Fig. 2.4). The cell selection and mode selection schemes use the RSRP calculation described in [36]. Table 5.1 summarizes the system level settings being used in this work. Figs. 5.1 and 5.2 illustrate the performance results for this 5G wireless HetNet system.

Table 5.1: System level simulation parameters

Parameter	Value	Parameter	Value
eNB-eNB distance	0.5 km	eNB antenna e-tilt	15^o
eNB antenna pattern	3D, sector antenna [36]	eNB antenna polarization	Vertical
eNB Tx Power	46 dBm	FAP Tx Power	30 dBm
eNB-UE channel	UMa [36]	FAP-UE channel	UMi [36]
UE deployment	Hot-spot (6 UEs/cluster)	Number of hot-spots	3 or 5 per sector
Number of UEs	1710 ($\sim$ 30/sector)	Number of FAPs	0, 3 or 5 per sector
UE antenna	Dipole	FAP antenna	MRA with 24 modes
Cell selection bias	Optimized over 0, 3, 6 and 9 dB	MRA modes	Diversity modes, Directive modes, Omni

Let us first investigate the SINR and throughput distributions. In Figs. 5.1.a and 5.1.b, we depict, for the case of planned FAP deployment, the empirical cumulative distribution function (CDF) of the SINR and throughput over 1710 UEs, respectively. As expected, significant improvements in both SINR and throughput is achieved by deploying FAPs to the system. In addition, the developed MRAs help further improve both SINR and throughput of the UEs. It is seen that with 5 FAP/sector, e.g., a denser FAP deployment, the SINR distribution becomes worse compared to that for 3 FAP/sector deployment, which is mainly due to increased FAP density resulting higher interference. However, the MRAs help reduce the resulting interference via the directive modes of operation and provide

about $2 - 2.5$ dB SINR improvement. In addition, for a denser FAP deployment, e.g., 5 FAPs/sector, more improvements with MRAs are observed. This is mainly due to the fact that the interference due to FAP transmissions increase, however the MRA system optimizes the radiation patterns such that appropriately directed beams towards the desired set of UEs are excited at each FAP. The off-loading effect combined with suitable modes of MRAs provides remarkable improvements to the system performance.

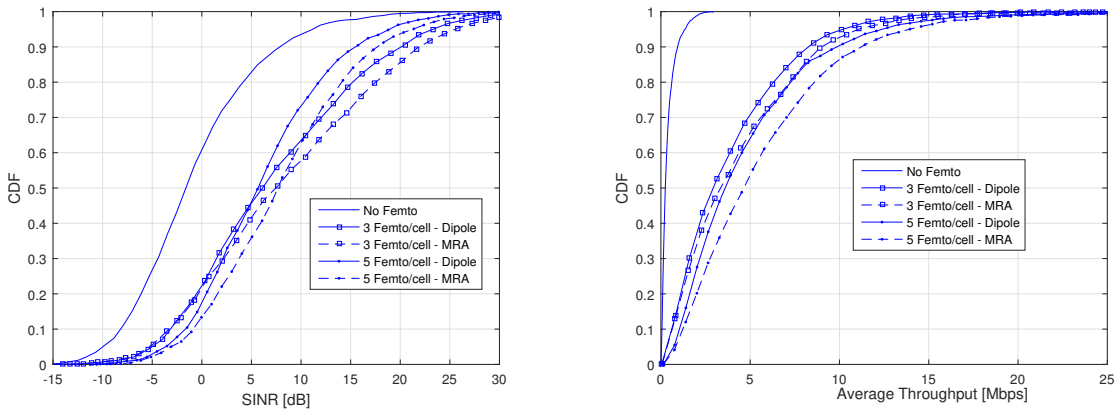

Fig. 5.1: Performance improvement with MRAs in HetNet, (a) cumulative distribution of SINR, (b) cumulative distortion of per user throughput.

In Fig. 5.2, we compare the average capacity and coverage performance for various systems. For comparison purposes, we include the case of no FAP in the system and the system with FAPs employing dipole antennas. The average capacity is defines as the average of 1710 UEs' Shannon rates evaluated using the resulting SINR values. For the coverage throughput, Γ_α, we set $\alpha = 0.05$, i.e., 5-percentile capacity coverage of the network. It is seen that in both planned and random FAP deployment, the MRAs at FAPs provide significant capacity gains and coverage improvements. For example, in the planned deployment, the MRA antennas provided an additional 29% per UE percent capacity gain and 13% coverage improvement over the gains from small cell deployment employing dipole antennas. Even for randomly positioned FAPs, for which the FAPs are randomly dropped any where in the 57-sector area, the MRA modes provide more than 10% capacity gains and

5% coverage improvements for both 3 and 5 FAP/sector. We note that in the simulations, omni-directional mode of operation is also included during mode selection optimization at FAPs. The omni-mode of operation becomes useful especially in random FAP deployment scenarios where UEs may be uniformly distributed within the coverage area of the FAP.

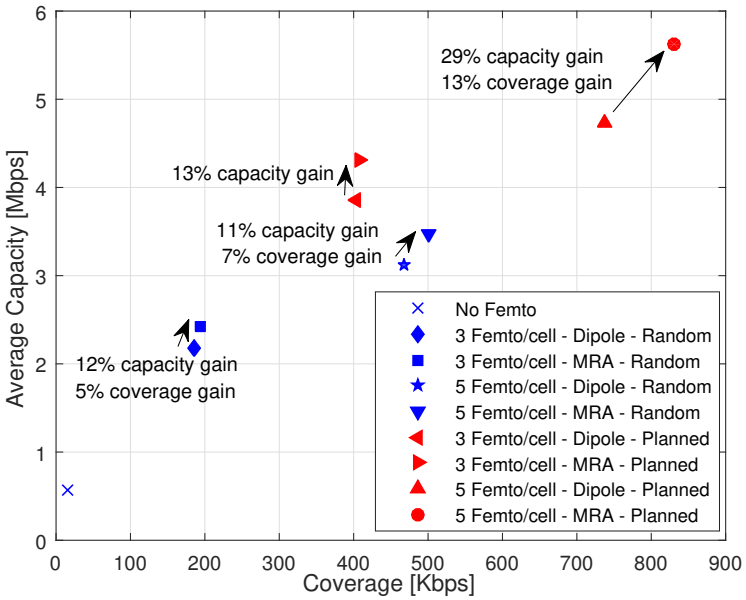

Fig. 5.2: Comparison of per UE capacity vs. 5−percentile throughput coverage. For both planned and random deployment, FAPs with MRAs provide performance improvement with distributed mode selection algorithm.

CHAPTER 6

CONCLUSION

A parasitic layer based multifunctional reconfigurable antenna (MRA) that is capable of 3D beam steering is developed. The presented reconfigurable antenna consists of a driven dipole element surrounded by a 3D parasitic enclosure comprising of small metallic pixels interconnected by PIN diode switches. With different switch states, the geometry of the parasitic surfaces can be modified to create various radiation patterns. The MRA geometry and the lumped components for switching circuitry are optimized to attain 360^o azimuthal beam steering and -18^o to 18^o elevation tilts along with several diversity patterns. These resulting patterns can effectively be utilized for interference management in 5G wireless heterogenous networks. The MRA has been fabricated and its resonance characteristics measured, which closely matched to full-wave analysis results. Assuming a typical 5G heterogenous network where the small cell access points are equipped with the presented MRA, a distributed low-complexity mode selection algorithm is developed. Using the system-level performance evaluation methodology of 5G networks by 3GPP, the capacity and coverage performance is studied. It is seen that up to 29% throughput gains and 13% coverage improvements can be attained. This work attempts to develop a unified approach with the goal of achieving 5G performance requirements, where antenna design, communications/signal processing and network aspects are seamlessly integrated, and the critical system parameters (environment, EM wave properties, and communication algorithms) are jointly optimized.

The presented single-element MRA is capable of creating desirable directive beam patterns in both azimuthal and elevation planes. An immediate future research direction is to extend this architecture to the case of reconfigurable MIMO antenna systems. Furthermore, other pixel shapes and parasitic enclosure geometries can be investigated to create polarization diverse patterns in addition to directionally diverse patterns. From our system level performance results, we see that the presented MRA have also significant consequences for

the design and optimization of 5G and beyond networks. For example, interference management, load balancing, and MRA mode design/selection can jointly be optimized to excel the 5G network performance.

REFERENCES

[1] D. Rodrigo, B. Cetiner, and L. Jofre, "Frequency, radiation pattern and polarization reconfigurable antenna using a parasitic pixel layer," *Antennas and Propagation, IEEE Transactions on*, vol. 62, no. 6, pp. 3422–3427, June 2014.

[2] Z. Li, D. Rodrigo, L. Jofre, and B. Cetiner, "A new class of antenna array with a reconfigurable element factor," *IEEE Transactions on Antennas and Propagation*, vol. 61, no. 4, pp. 1947–1955, April 2013.

[3] C. J. Panagamuwa, A. Chauraya, and J. C. Vardaxoglou, "Frequency and beam reconfigurable antenna using photoconducting switches," *IEEE Transactions on Antennas and Propagation*, vol. 54, no. 2, pp. 449–454, Feb 2006.

[4] C. Plapous, J. Cheng, E. Taillefer, A. Hirata, and T. Ohira, "Reactance domain music algorithm for electronically steerable parasitic array radiator," *IEEE Transactions on Antennas and Propagation*, vol. 52, no. 12, pp. 3257–3264, Dec 2004.

[5] X. Yuan, Z. Li, D. Rodrigo, H. Mopidevi, O. Kaynar, L. Jofre, and B. Cetiner, "A parasitic layer-based reconfigurable antenna design by multi-objective optimization," *IEEE Transactions on Antennas and Propagation*, vol. 60, no. 6, pp. 2690–2701, June 2012.

[6] N. Fourikis, *Phased array-based sytems and applications.* Newyork: Wiley, 1997.

[7] J. T. Nemit, "Network approach for reducing the number of phase shifters in a limited scan phased array," U.S. Patent 380 3625, 1974.

[8] A. Abbaspour-Tamijani and K. Sarabandi, "An affordable millimeter-wave beam-steerable antenna using interleaved planar subarrays," *IEEE Transactions on Antennas and Propagation*, vol. 51, no. 9, pp. 2193–2202, Sep 2003.

[9] R. Harrington, "Reactively controlled directive arrays," *IEEE Transactions on Antennas and Propagation*, vol. 26, no. 3, pp. 390–395, May 1978.

[10] C. Sun, A. Hirata, T. Ohira, and N. C. Karmakar, "Fast beamforming of electronically steerable parasitic array radiator antennas: theory and experiment," *IEEE Transactions on Antennas and Propagation*, vol. 52, no. 7, pp. 1819–1832, July 2004.

[11] B. Alshami, H. Aboulnour, and M. Dib, "Design of a broadband espar antenna," in *2009 Mediterrannean Microwave Symposium (MMS)*, Nov 2009, pp. 1–6.

[12] N. L. Scott, M. O. Leonard-Taylor, and R. G. Vaughan, "Diversity gain from a single-port adaptive antenna using switched parasitic elements illustrated with a wire and monopole prototype," *IEEE Transactions on Antennas and Propagation*, vol. 47, no. 6, pp. 1066–1070, Jun 1999.

[13] S. Lim, "Design of a multidirectional, high-gain compact yagi antenna," *IEEE Antennas and Wireless Propagation Letters*, vol. 8, pp. 418–420, 2009.

[14] R. Schlub and D. V. Thiel, "Switched parasitic antenna on a finite ground plane with conductive sleeve," *IEEE Transactions on Antennas and Propagation*, vol. 52, no. 5, pp. 1343–1347, May 2004.

[15] H. Kawakami and T. Ohira, "Electrically steerable passive array radiator (espar) antennas," *IEEE Antennas and Propagation Magazine*, vol. 47, no. 2, pp. 43–50, April 2005.

[16] P. D. Einziger, Y. Leviatan, and J. Rozenkovich, "Broad-band reactively loaded dipole antenna," *Microwave and Optical Technology Letters*, vol. 2, no. 6, pp. 208–210, 1989. [Online]. Available: http://dx.doi.org/10.1002/mop.4650020607

[17] T. Tanaka, F. Nakahara, S. Egashira, and A. Sakitani, "Determination method of the loading impedances of beam tilting antenna with passive loads," in *Antennas and Propagation Society International Symposium, 1997. IEEE., 1997 Digest*, vol. 3, July 1997, pp. 1604–1607 vol.3.

[18] H. Scott and V. F. Fusco, "Electronic beam tilting using a single reactively loaded circular wire loop antenna," *IEE Proceedings - Microwaves, Antennas and Propagation*, vol. 149, no. 56, pp. 271–274, Oct 2002.

[19] A. Alù, F. Bilotti, N. Engheta, and L. Vegni, "Subwavelength, compact, resonant patch antennas loaded with metamaterials," *IEEE Transactions on Antennas and Propagation*, vol. 55, no. 1, pp. 13–25, 2007.

[20] S. Ferdous, A. Hossain, S. M. H. Chowdhury, M. R. C. Mahdy, and M. Abdul, "Reduced and conventional size multi-band circular patch antennas loaded with metamaterials," *IET Microwaves, Antennas & Propagation*, vol. 7, no. 9, pp. 768–776, 2013.

[21] W. Liu, Z. N. Chen, and X. Qing, "Metamaterial-based low-profile broadband mushroom antenna," *IEEE Transactions on Antennas and Propagation*, vol. 62, no. 3, pp. 1165–1172, 2014.

[22] D. Li, Z. Szabo, X. Qing, E.-P. Li, and Z. N. Chen, "A high gain antenna with an optimized metamaterial inspired superstrate," *IEEE transactions on antennas and propagation*, vol. 60, no. 12, pp. 6018–6023, 2012.

[23] A. Dadgarpour, B. Zarghooni, B. S. Virdee, and T. A. Denidni, "Beam tilting antenna using integrated metamaterial loading," *IEEE Transactions on Antennas and Propagation*, vol. 62, no. 5, pp. 2874–2879, May 2014.

[24] ——, "Improvement of gain and elevation tilt angle using metamaterial loading for millimeter-wave applications," *IEEE Antennas and Wireless Propagation Letters*, vol. 15, pp. 418–420, 2016.

[25] I. Kim and Y. Rahmat-Samii, "Electromagnetic band gap-dipole sub-array antennas creating an enhanced tilted beams for future base station," *IET Microwaves, Antennas Propagation*, vol. 9, no. 4, pp. 319–327, 2015.

[26] D. Rodrigo, L. Jofre, and B. A. Cetiner, "Circular beam-steering reconfigurable antenna with liquid metal parasitics," *IEEE Transactions on Antennas and Propagation*, vol. 60, no. 4, pp. 1796–1802, April 2012.

[27] R. H. MacPhie and S. K. Darbha, "The input impedance of a thin dipole with sinusoidal surface current distribution by the poynting vector method," *IEEE Transactions on Antennas and Propagation*, vol. 43, no. 11, pp. 1336–1339, Nov 1995.

[28] C. A. Balanis, *Antenna Theory: Analysis and Design.* Wiley-Interscience, 2005.

[29] Z. Li, E. Ahmed, A. M. Eltawil, and B. A. Cetiner, "A beam-steering reconfigurable antenna for wlan applications," *IEEE Transactions on Antennas and Propagation*, vol. 63, no. 1, pp. 24–32, Jan 2015.

[30] D. Cheng and C. Chen, "Optimum element spacings for yagi-uda arrays," *IEEE Transactions on Antennas and Propagation*, vol. 21, no. 5, pp. 615–623, Sep 1973.

[31] M. Unlu, M. Hashemi, C. Berry, S. Li, S.-H. Yang, and M. Jarrahi, "Switchable scattering meta-surfaces for broadband terahertz modulation," *Scientific reports*, vol. 4, 2014.

[32] J. Rodriguez, *Fundamentals of 5G Mobile Networks.* John Wiley and Sons, 2015.

[33] H. S. Dhillon, R. K. Ganti, F. Baccelli, and J. G. Andrews, "Modeling and analysis of k-tier downlink heterogeneous cellular networks," *IEEE Journal on Selected Areas in Communications*, vol. 30, no. 3, pp. 550–560, April 2012.

[34] 3GPP, "TR 36.932: Scenarios and requirements for small cell enhancements for E-UTRA and E-UTRAN (Rel. 13)," [Online]. Available: http://www.3gpp.org/ftp/Specs/archive/36_series/ 36.932/36932-d00.zip, Dec 2015.

[35] C. Oestges and B. Clerckx, *MIMO Wireless Communications: From Real-World Propagation to Space-Time Code Design.* Elsevier Science, 2010.

[36] 3GPP, "TR 36.873: Study on 3D channel model for LTE (Rel. 12)," [Online]. Available: http://www.3gpp.org/ftp/Specs/archive/ 36_series/36.873/36873-c20.zip, June 2015.

[37] S. Mukherjee, "Distribution of downlink sinr in heterogeneous cellular networks," *IEEE Journal on Selected Areas in Communications*, vol. 30, no. 3, pp. 575–585, April 2012.

[38] N. Prasad, M. Arslan, and S. Rangarajan, "Exploiting cell dormancy and load balancing in LTE HetNets: Optimizing the proportional fairness utility," *IEEE Transactions on Communications*, vol. 62, no. 10, pp. 3706–3722, Oct 2014.

[39] E. Dahlman, S. Parkvall, and J. Skold, *4G: LTE/LTE-Advanced for Mobile Broadband.* Elsevier Science, 2013.

[40] H. S. Dhillon and J. G. Andrews, "Downlink rate distribution in heterogeneous cellular networks under generalized cell selection," *IEEE Wireless Communications Letters*, vol. 3, no. 1, pp. 42–45, February 2014.

[41] A. K. Gupta, H. S. Dhillon, S. Vishwanath, and J. G. Andrews, "Downlink multi-antenna heterogeneous cellular network with load balancing," *IEEE Transactions on Communications*, vol. 62, no. 11, pp. 4052–4067, Nov 2014.

[42] X. Chu, D. López-Pérez, Y. Yang, and F. Gunnarsson, *Heterogeneous Cellular Networks: Theory, Simulation and Deployment*. Cambridge University Press, 2013.

[43] 3GPP, "Draft for TR 38.802: Study on new radio ((nr)) access technology physical layer aspects (Rel. 14)," [Online]. Available: http://www.3gpp.org/ftp/TSG_RAN/WG1_RL1/TSGR1_86b /Docs/R1-1610848.zip, Oct 2016.

CURRICULUM VITAE

Mohammad Ababil Hossain

Journal Articles

- Md. Ababil Hossain, Israfil Bahceci, and Bedri A. Cetiner, "Parasitic Layer Based Radiation Pattern Reconfigurable Antenna for 5G Communications", in the special issue of Oct. 2016 of *IEEE Transactions on Antennas and Propagation* (accepted with revision).